Title	Computational study of the influence of microstructure on fracture behavior near crack-tip field in nacre-like materials
Author(s)	Ye, Xiaoyan; Nakatani, Akihiro
Citation	Mechanics of Materials. 2024, 195, p. 105034
Version Type	VoR
URL	https://hdl.handle.net/11094/97649
rights	This article is licensed under a Creative Commons Attribution 4.0 International License.
Note	

Contents lists available at ScienceDirect

Mechanics of Materials

Research paper

Computational study of the influence of microstructure on fracture behavior near crack-tip field in nacre-like materials

Xiaoyan Ye, Akihiro Nakatani *

Division of Mechanical Engineering, Graduate School of Engineering, Osaka University, 2-1 Yamadaoka, Suita, 565-0871, Osaka, Japan

ARTICLE INFO

ABSTRACT

The small-scale failure process around a plane strain mode I crack in nacre-like materials is analyzed. The displacement increments of boundary nodes are specified by the analytical solutions based on the orthotropic linear elasticity to conduct an incremental finite element analysis. We set up a structural model composed of staggered arranged brittle aragonite tablets and cohesive zones within a process window surrounding the crack tip to investigate the toughness as well as the deformation mechanism in the fracture process zone. The results obtained by the parametric studies of different geometries and mechanical properties in the microstructure of the materials show that the aspect of failure in the near-tip fields can be categorized into four distinct fracture mechanisms. These mechanisms significantly affect the fracture toughness with differences of hundreds of times. We show a failure-mechanism map in which these fracture mechanisms can be divided into regions of geometry and mechanical properties in microstructure. Findings obtained in this study about the toughening mechanisms give us the useful knowledge to design novel materials with specific microstructures to control fracture mechanisms.

1. Introduction

Recently, researchers have attempted to uncover the underlying correlations between the macroscopic properties and microstructural features of biological materials, such as nacre-like materials, to provide new inspiration and design guidelines for engineering applications. Nacre-like materials are a class of natural composites that exhibit similar microstructure and mechanical properties, including nacre, osteon, dentin, and others. For example, nacre is a natural material found in the inner layer of the shells that protects the underlying soft tissue from external threats and attacks. Nacre comprises approximately 95 wt% of staggered arranged brittle aragonite tablets and 5 wt% of proteins that connect adjacent tablets (Wang et al., 2001; Wang and Gupta, 2011; Barthelat et al., 2006). Distinctive deformation of nacre occurs through relative sliding between tablets when subjected to tensile loading parallel to the tablets (Barthelat et al., 2007). Notably, a mere 5 wt% of proteins in nacre results in a remarkable enhancement in fracture toughness, ranging from 40 to 3000 times higher than that of pure aragonite, when exposed to tensile loading parallel to the tablets (Mayer, 2006), which is accompanied by a minor reduction in strength and stiffness (Sun and Bhushan, 2012). Similar findings have been reported for other types of nacre-like materials with similar staggered microstructures, including osteon (Vashishth, 2004) and

dentin (Kruzic et al., 2003). This remarkable balance has attracted research attention, resulting in investigations on the connection between the macroscopic mechanical properties and microstructure.

Numerous toughening mechanisms have been identified for nacre-like materials in recent years. At the nanoscale, nanoasperities on the surfaces of aragonite tablets (Wang et al., 2001; Barthelat et al., 2006), mineral bridges (Meyers et al., 2008), the interlocking effect (Barthelat et al., 2007), and the deformation strengthening of proteins (Ji and Gao, 2004) have been identified as toughening mechanisms of nacre-like materials. These features restrain the relative sliding between the tablets, increasing energy dissipation during crack propagation and enhancing toughness. Additionally, microscale toughening mechanisms are significant. Significant energy dissipation occurring in the sizable nonelastic region of a process zone near the crack tip during crack propagation is recognized as the crucial origin of toughness (Barthelat, 2010; Barthelat and Rabiei, 2011). Crack morphology is also related with toughening, e.g. crack deflections (Menig et al., 2000; Abid et al., 2019; Xie and Yao, 2014), crack branches (Wang et al., 1995), and microcracks (Sarikaya et al., 1989). The artificial design and activation of these toughening mechanisms to achieve optimal toughness in artificial nacre-like materials remain challenging.

Computer simulations are crucial for in-depth investigation of the toughening mechanisms of nacre-like materials. Various simulation

---

methods have been used, including the finite element analysis (Rabiei et al., 2010; Maghsoudi-Ganjeh et al., 2021; Yan et al., 2022), phase-field method (Tsai et al., 2021), and Monte Carlo annealing (Yan and Nakatani, 2019a, 2020). Most simulations can only be performed on tens to hundreds of tablets because of the problematic computational costs posed by the complex staggered microstructure and nonlinear interface properties. Such a model scale is insufficient for studying the dynamic failure process, because it fails to completely capture the mechanical behavior within the process zone near the crack tip. Therefore, reducing the computational costs becomes an unavoidable challenge when delving deeper into the study of toughening mechanisms. In studies by Abid et al. (2018, 2019), the discrete element method was employed to upscale the model to hundreds of thousands of tablets, investigating the influence of tablet overlap and the randomness of the microstructure on the mechanical properties. The effects of interface properties and tablet orientation on the near-tip field and crack initiation in nacre-like materials is studied by Pro et al. (2015a) using a GPU-based Monte Carlo annealing method and scaled up the model to hundreds of thousands of tablets.

Nevertheless, many aspects of the toughening mechanisms in nacre-like materials remain elusive. Fracture process under small-scale yielding (SSY) conditions is crucial for understanding and predicting the behavior of materials (Nakatani et al., 2003; Roychowdhury and Dodds, 2003). However, most of the previous studies for nacre-like materials have been conducted using simplified models, such as uniaxial tensile loading, assumption of rigid tablets, periodic boundary condition etc., for the sake of computational efficiency. These simplified models are sophisticated and effective to investigate an ideal strength coming from the intrinsic microstructure, but they are not directly applicable to the study of highly concentrated stress field near the crack tip, in which mesoscopic fracture mechanisms are closely related to the origins of the exceptional mechanical properties of nacre-like materials.

In this study we adopt the finite element method to investigate the deformation and failure behavior near the crack-tip field of nacre-like materials under SSY conditions. First, an SSY model combining structural and continuum-homogenized models is proposed. We focus on the near-tip field and fracture process in the process zone while homogenizing the elastic region far from the crack tip as an orthotropic material. The proposed model balances the retained analysis accuracy near the crack tip and it is a surrogate model of large scale model composed of millions of tablets. Furthermore, we identify four distinct fracture mechanisms by varying the aspect ratio of the tablets and interface properties. These mechanisms exhibit different sizes and shapes of the process zone, diverse crack morphologies, various near-tip fields, and hundreds of times differences in overall toughness. We also discuss the design principles of microstructure that induce specific fracture mechanisms and activate specific toughening mechanisms. This research reveals how microstructure affects the fracture mechanisms and overall toughness of nacre-like materials and provides valuable insights for designing artificial nacre-like materials.

2. Model and methods

2.1. Periodic microstructure

In this study, we model a two-dimensional periodic structure inspired by the staggered structure of natural nacre-like materials, as shown in Fig. 1. The uniaxial tension parallel with the vertical axis is dominant in stress field under the plane strain condition, as mode I crack is set along the horizontal axis in this study (see 2.3). The specimen consists of tablets which are simplified as isotropic elastic material specified by Young's modulus E and Poisson's ratio ν, whereas the crystal orientation, nanoasperities, and mineral bridges are neglected. The tablets have a length of l and a width of w, resulting in an aspect ratio of $k = l/w$. Furthermore, we define the characteristic angle $\theta' = \arctan(k/2)$. Geometrically, θ' denotes the angle between the
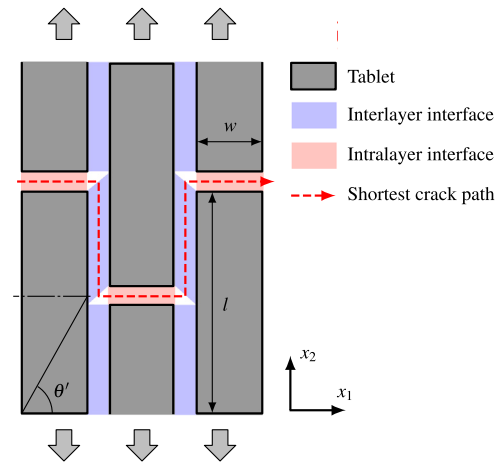

Fig. 1. Schematic diagram of the periodic staggered microstructure used in the finite element analysis. Each tablet is modeled using a four-node bulk element, while each interface is modeled by several four-node cohesive zone elements.

half-tablet diagonal and the x_1-axis and physically corresponds to the shortest crack path passing through a layer of the staggered structure, as shown in Fig. 1. For simplicity, the influence of tablets' overlap is not considered in this study, indicating that the end of any tablet coincides with the midpoint of the tablet in adjacent layers.

The interfaces can be categorized into two types based on their positions (i.e., intralayer and interlayer interfaces) to investigate the influence of interface properties more thoroughly, as shown in Fig. 1.

The finite element method is utilized to simulate both deformation and failure in the model. Considering the deformation process of nacre-like materials, the deformation of the tablets is significantly limited (Abid et al., 2019), in this study, each tablet is considered as an integral unit and represented by a four-node bulk element. The interfaces are modeled using the cohesive zone model (see 2.2), where each interface is segmented into several four-node cohesive zone elements.

2.2. Cohesive zone model and damage parameter

Experimental observations reveal the restraining effect of a complicated staggered structure on the crack propagation path in nacre-like materials (Wang et al., 1995). Rather than propagating through the tablets, cracks tend to follow the tortuous interfaces between the tablets, leading to the failure of the protein matrix. The cohesive zone (CZ) model is well-suited for cases where the crack path is predetermined in materials like nacre. Hence, the CZ model has been widely used in studies on nacre-like materials (Yan and Nakatani, 2019a,b; Pro et al., 2015b). Therefore, in this study, we neglect the fracture of the tablets and employ the CZ model to analyze the fracture of both the interlayer and intralayer interfaces.

According to the CZ model, the constitutive relationship of the interfaces is defined in terms of the nonlinear relationship between the traction T and separation Δ, called the cohesive law. The tangential and normal components of separation and traction are divided as $\Delta = (\Delta_t, \Delta_n)$ and $T = (T_t, T_n)$, denoted by the subscripts 't' (tangential) and 'n' (normal), respectively. A sophisticated cohesive law is proposed by Xu and Needleman (1994), in which the cohesive law can be derived from a potential function $\phi(\Delta)$, and it is utilized with following its fundamental concept in our present formulation. However, we neglect the coupling effect between tangential and normal separations for the sake of simplicity, and assume the potential functions as follows:

$$
\begin{aligned}
\phi_t(\Delta_t) &= \left[1 - \exp\left(-\frac{\Delta_t^2}{\Delta_t^{cr\,2}} \right) \right] \phi_0, \\
\phi_n(\Delta_n) &= \left[1 - \exp\left(-\frac{\Delta_n}{\Delta_n^{cr}} \right) \left(1 + \frac{\Delta_n}{\Delta_n^{cr}} \right) \right] \phi_0
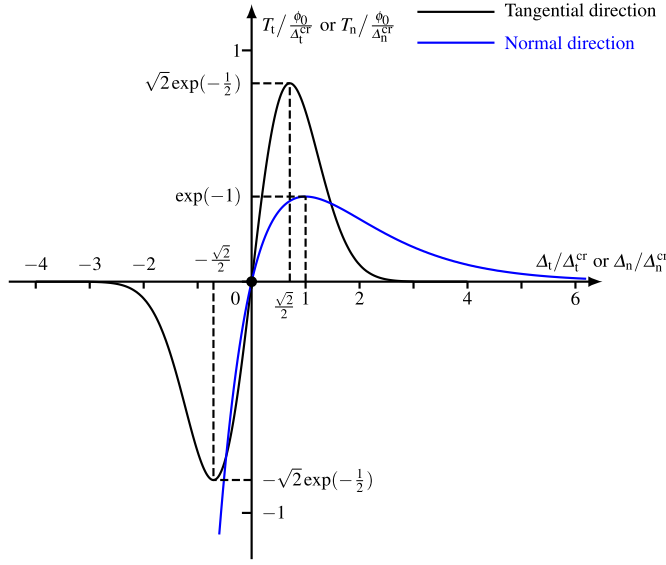\end{aligned}
\tag{1}
$$

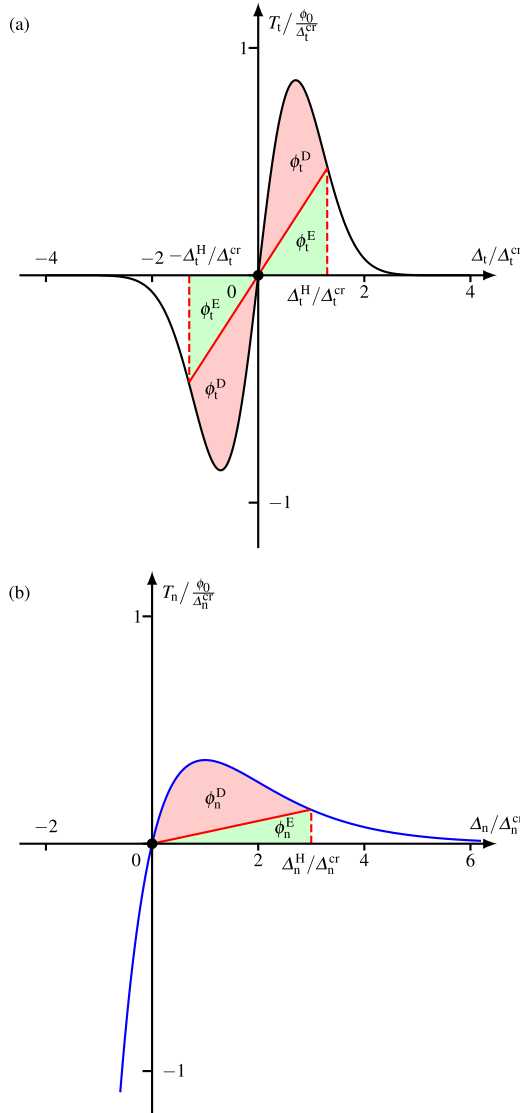Fig. 2. The cohesive law employed in this study.

Fig. 3. Unloading behavior of the cohesive law: (a) Tangential direction. (b) Normal direction.

For the simplicity, we adopt a commonly used assumption in the formulation of unified potential-based cohesive laws, in which the fracture energies in the tangential and normal directions are considered equivalent and denoted by the symbol ϕ_0 (Xu and Needleman, 1994; Zavattieri et al., 2008). Then we obtain the cohesive law on the fundamental path for increasing separation as follows:

$$T_t(\Delta_t) = \frac{d\phi_t}{d\Delta_t} = 2\frac{\phi_0}{\Delta_t^{cr}}\frac{\Delta_t}{\Delta_t^{cr}}\exp\left(-\frac{\Delta_t^2}{\Delta_t^{cr\,2}}\right),$$

$$T_n(\Delta_n) = \frac{d\phi_n}{d\Delta_n} = \frac{\phi_0}{\Delta_n^{cr}}\frac{\Delta_n}{\Delta_n^{cr}}\exp\left(-\frac{\Delta_n}{\Delta_n^{cr}}\right) \tag{2}$$

where Δ_t^{cr} and Δ_n^{cr} are critical separations in the tangential and normal directions, respectively. The cohesive law normalized by ϕ_0/Δ_t^{cr}, ϕ_0/Δ_n^{cr} and Δ_t^{cr}, Δ_n^{cr} are presented in Fig. 2. The traction changes nonlinearly with increasing separation, initially increasing and then steadily decreasing, approaching zero, mimicking the nonlinear failure behavior of the interface. The maximum tractions in the tangential and normal directions are expressed as follows:

$$T_t^{max} = \sqrt{2}\frac{\phi_0}{\Delta_t^{cr}}\exp\left(-\frac{1}{2}\right),$$

$$T_n^{max} = \frac{\phi_0}{\Delta_n^{cr}}\exp(-1) \tag{3}$$

Now we can rewrite the cohesive law Eq. (2) using three parameters, Δ_t^{cr}, Δ_n^{cr}, and T_n^{max} explicitly as

$$T_t(\Delta_t) = 2\,T_n^{max}\frac{\Delta_n^{cr}}{\Delta_t^{cr}}\frac{\Delta_t}{\Delta_t^{cr}}\exp\left(1 - \frac{\Delta_t^2}{\Delta_t^{cr\,2}}\right),$$

$$T_n(\Delta_n) = T_n^{max}\frac{\Delta_n}{\Delta_n^{cr}}\exp\left(1 - \frac{\Delta_n}{\Delta_n^{cr}}\right) \tag{4}$$

The history dependence of the cohesive zone such as damage effect must be considered due to the widespread occurrence of protein unloading during crack propagation in nacre-like materials (Rabiei et al., 2010). Under a linear unloading assumption of the cohesive zone as shown in Fig. 3, the traction-separation relationship during unloading process is expressed as

$$T_t^{unload}(\Delta_t) = \frac{\Delta_t}{\Delta_t^H}T_t(\Delta_t^H) \qquad (\Delta_t < \Delta_t^H),$$

$$T_n^{unload}(\Delta_n) = \frac{\Delta_n}{\Delta_n^H}T_n(\Delta_n^H) \qquad (\Delta_n < \Delta_n^H) \tag{5}$$

where Δ_t^H and Δ_n^H denote the experienced maximum (historically largest) separations in the tangential and normal directions, respectively. As the experienced maximum separation increases, a portion of the work done by the external forces is stored as elastic energy, denoted by ϕ_t^E and ϕ_n^E,

$$\phi_t^E(\Delta_t^H) = \frac{1}{2}\Delta_t^H T_t(\Delta_t^H),$$

$$\phi_n^E(\Delta_n^H) = \frac{1}{2}\Delta_n^H T_n(\Delta_n^H) \tag{6}$$

whereas the other portion is dissipated because of irreversible damage, denoted by ϕ_t^D and ϕ_n^D. ϕ_t^E and ϕ_n^E is represented by the triangular region between the unloading line and the horizontal axis, as shown in Fig. 3. The region between the loading and unloading lines represents the irreversible energy dissipation per unit area of the cohesive zone caused by the historical loading. We define a damage factor D to quantify the level of damage in the CZ, where D is the ratio of the dissipation energy to the fracture energy ϕ_0. Specifically, the dissipation energy corresponds to the area denoted by the symbols ϕ_t^D and ϕ_n^D in Fig. 3, and the damage factors for the tangential and normal CZ are estimated as follows:

$$D_t(\Delta_t^H) = \frac{\phi_t^D}{\phi_0} = \frac{1}{\phi_0}\left[\phi_t(\Delta_t^H) - \phi_t^E(\Delta_t^H)\right],$$

$$D_n(\Delta_n^H) = \frac{\phi_n^D}{\phi_0} = \frac{1}{\phi_0}\left[\phi_n(\Delta_n^H) - \phi_n^E(\Delta_n^H)\right] \tag{7}$$
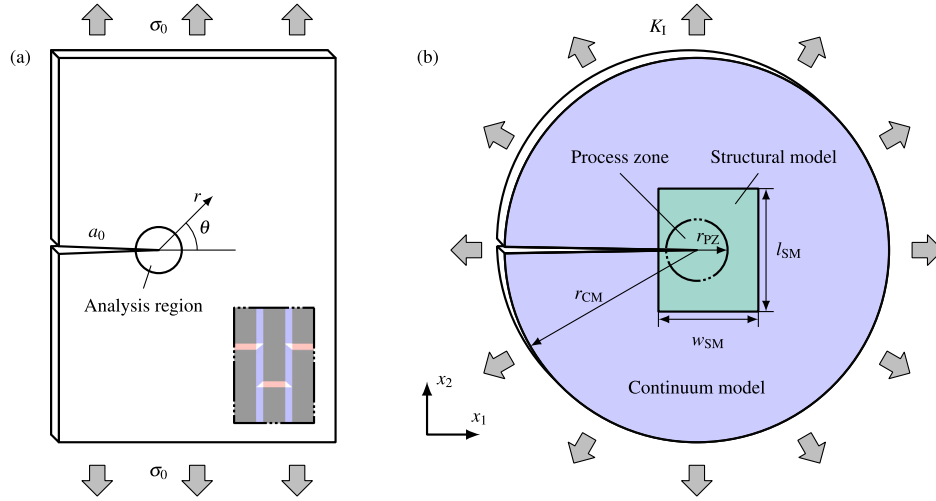
Fig. 4. Mode I small-scale yielding framework for modeling near crack-tip field in nacre-like materials. (a) Schematic illustration of mode I specimen. (b) Schematic illustration of analysis model composed of structural model and surrounding continuum model specified by stress intensity factor K_I.

For interlayer interfaces CZ_{inter}, $D = D_t(\Delta_t^H)$ and intralayer interfaces CZ_{intra}, $D = D_n(\Delta_n^H)$, because shear deformation predominates on interlayer interfaces, whereas tensile deformation predominates on intralayer interfaces in this study as shown schematically in Fig. 1.

For any given direction, D is equal to 0 when the CZ does not experience any loading. The damage accumulates and D gradually approaches 1 as the experienced maximum separation increases. From Fig. 3, it is apparent that the variable D exhibits a bounded range of $0 \leq D < 1$. In this study, we consider $D_f = 0.99$ as the criterion for CZ fracture. Given that the traction of both directions becomes negligibly small when D reaches 1, the sensitivity of $D_f = 0.99$ influence to results is sufficiently small. When one direction fractures, traction in the other direction is released, and the stiffness is set to 0.

2.3. Model of crack tip field under small-scale yielding condition

We focus on the mechanical response of nacre-like materials near crack-tip field. As shown in Fig. 4(a), we consider a semi-infinite plate with staggered microstructure and an edge crack of length a_0 that is perpendicular to the tablet direction and located in the center. Deformation occurs under a uniform remote tensile stress σ_0 parallel to the tablet direction. We assume singular stress field under SSY conditions of mode I crack in plane strain condition in which the stress intensity factor K_I predicts the near crack-tip stress field. To be precise, inelastic failure near crack-tip in the nacre-like materials is not expressed as 'yield'. From a viewpoint of the fracture mechanics, however, small-scale failure assumption near the crack tip can be regarded as the SSY condition. We select a circular region centered at the pre-crack tip as the analysis region for this study. More details are shown in Fig. 4(b).

For the SSY model, the analysis region should be significantly larger than the process zone. Considering the size of the process zone observed in nacre-like materials (Barthelat and Espinosa, 2007), the analysis region should be extremely large. However, the finite element model frequently possesses an extremely large bandwidth due to the complex staggered structure of nacre-like materials, which poses challenges for large-scale simulations. To reduce the computational costs, we divide the analysis region into two parts: the structural model (SM) inside a process window surrounding the crack tip and the continuum model (CM) away from the crack tip, as shown in Fig. 4(b). The fracture process zone is assumed to be confined inside the process window, in the same way to the discrete dislocation analysis of crack growth by Cleveringa et al. (2000) and Nakatani et al. (2003). The staggered structure is retained only in the SM, whereas the CM is homogenized into an orthotropic linear elastic material (Bertoldi et al.,

2008). The finite element mesh used in this study is shown in Fig. 5. The protein matrix filling between tablets is simplified as a four-node interface element.

The SM is adopted for a rectangular region surrounding the crack tip with a length of l_{SM} and a width of w_{SM}, preserving the microstructure shown in Fig. 1.

We examine the different microstructures of the nacre-like materials in a variety of two parameters that address both the geometric and mechanical characteristics. First, we set the width of the tablets, w, to be constant, whereas the geometric characteristics of the microstructure are specified by the aspect ratio k. In addition, different cohesive laws are employed to describe the intralayer and interlayer interfaces to comprehensively investigate the influence of the interfaces on the fracture behavior of nacre-like materials. We define a ratio, $p = T_{n, intra}^{max}/T_{n, inter}^{max}$, in which $T_{n, intra}^{max}$ and $T_{n, inter}^{max}$ denote the maximum normal tractions of intralayer interface and of interlayer interface, respectively. For simplicity, we maintain equal values of Δ_t^{cr} and Δ_n^{cr} for both intralayer and interlayer interfaces. This assumption allows us to characterize the interface properties of the model using a single parameter p. Note p also represents the ratio of the normal stiffness between the intralayer and the interlayer interfaces. Because $T_{n, inter}^{max}$ is set to a nonzero constant, as shown in Table 1, a higher value of p indicates a stronger intralayer connection. The model contains only interlayer connections when $p = 0$, similar to the widely used shear-lag model (Gao et al., 2003). For $p > 0$, intralayer connections are also considered, resulting in the classical brick-and-mortar model (Begley et al., 2012).

In contrast, for the CM, we simplify the periodic microstructure shown in Fig. 1 as a homogenized orthotropic linear elastic continuum. The components of homogenized compliance matrix, b_{IJ} for the CM are obtained from trial simulations, as shown in Appendix A. Under the SSY assumption, the boundary of the CM is dominated by the mode I stress intensity factor K_I. The boundary condition is given by the displacement increments of the boundary nodes, which are obtained from the theoretical displacement field of a linear elastic orthotropic material (Sih et al., 1965; Nejati et al., 2021).

$$u_1 = K_I \sqrt{\frac{2r}{\pi}} \mathrm{Re} \left[\frac{1}{\mu_1 - \mu_2} \left(\mu_1 p_2 \sqrt{\cos\theta + \mu_2 \sin\theta} - \mu_2 p_1 \sqrt{\cos\theta + \mu_1 \sin\theta} \right) \right],$$

$$u_2 = K_I \sqrt{\frac{2r}{\pi}} \mathrm{Re} \left[\frac{1}{\mu_1 - \mu_2} \left(\mu_1 q_2 \sqrt{\cos\theta + \mu_2 \sin\theta} - \mu_2 q_1 \sqrt{\cos\theta + \mu_1 \sin\theta} \right) \right]$$
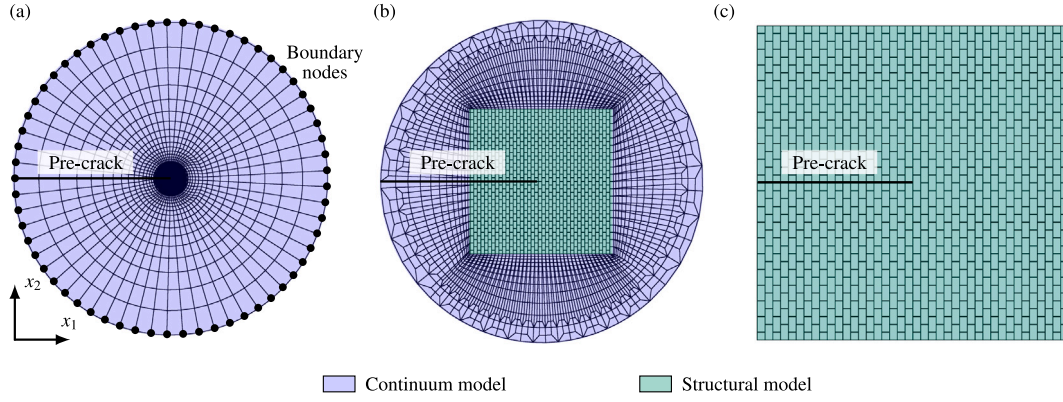
(8)

Fig. 5. Typical finite element mesh used in this study. From left to right, there is a continuous decrease in the magnification factor: (a) Homogenized continuum model. (b) Transition from outer circular continuum model to near-tip rectangular structural model inside the process window. (c) Structural model containing the staggered structure.
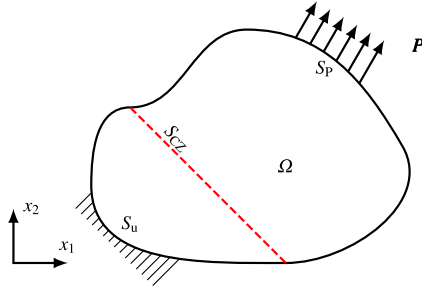

Fig. 6. Boundary value problem of a continuum body with a cohesive interface.

where (r, θ) represent the polar coordinates of the node, as shown in Fig. 4(a). The complex or purely imaginary number, μ_1 and μ_2, as well as their complex conjugates, $\bar{\mu}_1$ and $\bar{\mu}_2$, are the roots of the following equation:

$$b_{11}\mu^4 - 2b_{16}\mu^3 + \left(2b_{12} + b_{66}\right)\mu^2 - 2b_{26}\mu + b_{22} = 0 \tag{9}$$

p_j and q_j are given by

$$
\begin{aligned}
p_j &= b_{11}\mu_j^2 + b_{12} - b_{16}\mu_j, \\
q_j &= b_{12}\mu_j + \frac{b_{22}}{\mu_j} - b_{26}
\end{aligned}
\tag{10}
$$

where $j = 1, 2$. For the orthotropic material in the present coordinates, $b_{16} = b_{26} = 0$. Similarly, we can obtain a linear elastic stress field for orthotropic materials.

$$
\begin{aligned}
\sigma_{11} &= \frac{K_I}{\sqrt{2\pi r}} \operatorname{Re}\left[\frac{\mu_1\mu_2}{\mu_1 - \mu_2}\left(\frac{\mu_2}{\sqrt{\cos\theta + \mu_2\sin\theta}} \right.\right. \\
&\qquad\qquad \left.\left. - \frac{\mu_1}{\sqrt{\cos\theta + \mu_1\sin\theta}} \right)\right], \\
\sigma_{22} &= \frac{K_I}{\sqrt{2\pi r}} \operatorname{Re}\left[\frac{1}{\mu_1 - \mu_2}\left(\frac{\mu_1}{\sqrt{\cos\theta + \mu_2\sin\theta}} \right.\right. \\
&\qquad\qquad \left.\left. - \frac{\mu_2}{\sqrt{\cos\theta + \mu_1\sin\theta}} \right)\right], \\
\sigma_{12} &= \frac{K_I}{\sqrt{2\pi r}} \operatorname{Re}\left[\frac{\mu_1\mu_2}{\mu_1 - \mu_2}\left(\frac{1}{\sqrt{\cos\theta + \mu_1\sin\theta}} \right.\right. \\
&\qquad\qquad \left.\left. - \frac{1}{\sqrt{\cos\theta + \mu_2\sin\theta}} \right)\right]
\end{aligned}
\tag{11}
$$

The key parameters are chosen based on experimental observations (Barthelat et al., 2006; Li et al., 2004; Shao et al., 2014; Lin and Meyers, 2009), and the parameters of the model and simulation are listed in Table 1.

Table 1
Parameters of the model and simulation.

Parameters of tablet			
Dimensions	Width w [nm]	Length l [nm]	
	400	400 k	
Material	Young's modulus	Poisson's ratio	
parameters	E [GPa]	ν	
	80	0.3	
Parameters of interfaces			
Cohesive zone parameters of	Δ_t^{cr} [nm]	Δ_n^{cr} [nm]	T_n^{max} [MPa]
Interlayer interface CZ$_{inter}$	5	5	30
Intralayer interface CZ$_{intra}$	5	5	30 p
Boundary condition			
Displacement components at boundary nodes of the model for the updated K_I are specified by Eq. (8)			
Key parameters for parametric study			
p: ratio of maximum normal tractions varied in range of 0 to 30			
k: aspect ratio of tablets varied in the range of 2 to 40			

The analysis model involves an SM region comprising a total of 70 layers, each consisting of 50 tablets, which have a size of 50×70, and the size of the CM, r_{CM}, is more than 100 times larger than that of the SM. From trial simulations as shown in Appendix B, we understand that the fracture behavior within the process zone of the characteristic length, r_{PZ}, remains independent of the SM size at this scale, and the chosen dimensions of models ensure that the influence of nonlinear deformation near the crack tip on the boundaries of the CM is negligible and validating the SSY conditions.

3. Computational implement and post-processing

3.1. Incremental finite element method

In this study, the boundary value problem of a continuum body Ω involving the CZ interface S_{CZ} as shown in Fig. 6 is solved using the finite element method based on the incremental form of the principle of virtual work. The displacement $\boldsymbol{u}$ and the external load $\boldsymbol{P}$ are specified on the boundaries S_u and S_P, respectively. The rate form of the principle of virtual work at time t

$$\int_\Omega \dot{\sigma}_{ij}\delta\varepsilon_{ij}\mathrm{d}V = \int_{S_{CZ}} \left(\dot{T}_n\delta\Delta_n + \dot{T}_t\delta\Delta_t\right)\mathrm{d}S + \int_{S_P} \dot{P}_i\delta u_i\mathrm{d}S \tag{12}$$

holds, where $(\dot{})$ is the material time derivative, σ_{ij} is the stress tensor, ε_{ij} is the strain tensor, u_i is the displacement vector, and P_i is a component of external force $\boldsymbol{P}$. For the crack problem, traction free condition $P_i = 0$ is set on the pre-crack surface. Increment of the nodal displacement under loading can be specified for the boundary condition of the incremental finite element calculation based on Eq. (12).
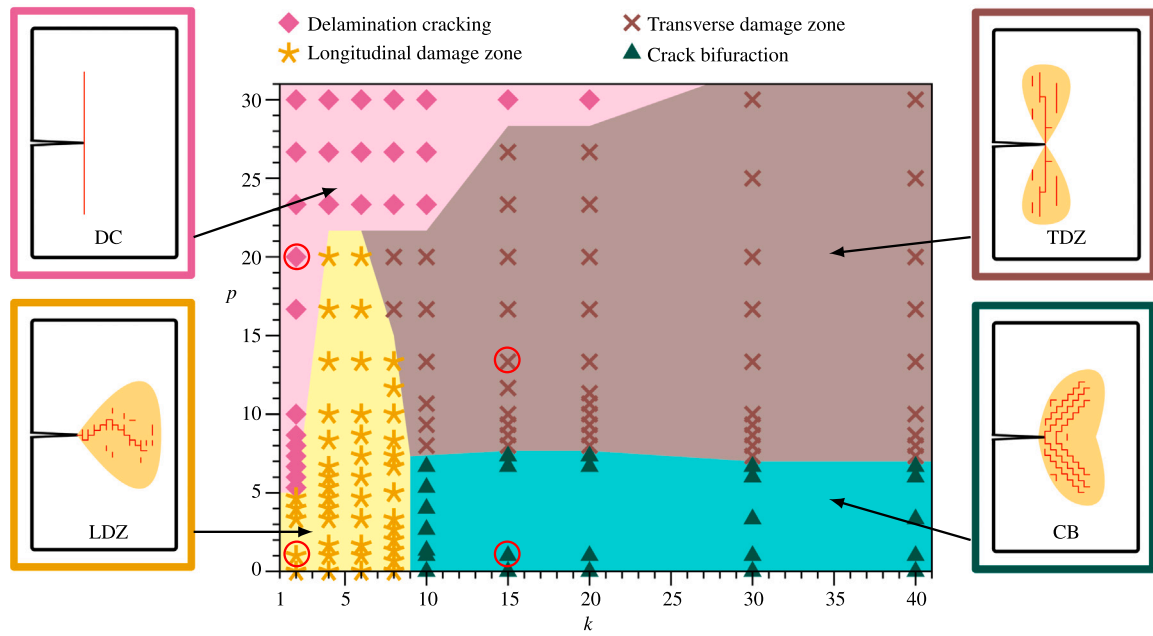
Fig. 7. Failure-mechanism map: fracture mechanism transition induced by microstructural changes. (For interpretation of the references to color in this figure legend, the reader is referred to the web version of this article.)
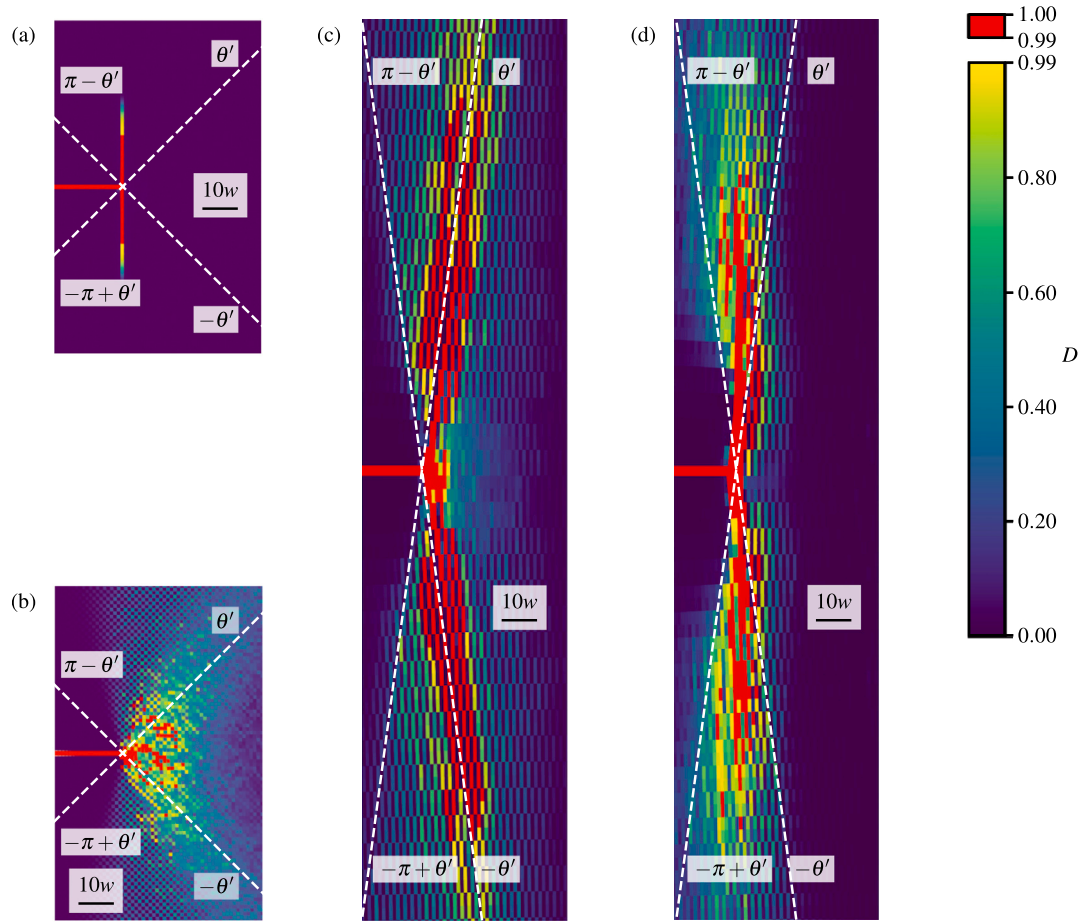

Fig. 8. The characteristics of the process zone and the energy dissipation within it, as represented by the D. (a) Delamination cracking mechanism ($k = 2$, $p = 20$, $K_I = 14.5$ GPa$\sqrt{\text{nm}}$, $w_{SM} = 28\,000$ nm, $l_{SM} = 40\,000$ nm). (b) Longitudinal damage zone mechanism ($k = 2$, $p = 1$, $K_I = 41.7$ GPa$\sqrt{\text{nm}}$, $w_{SM} = 28\,000$ nm, $l_{SM} = 40\,000$ nm). (c) Crack bifurcation mechanism ($k = 15$, $p = 1$, $K_I = 151.6$ GPa$\sqrt{\text{nm}}$, $w_{SM} = 28\,000$ nm, $l_{SM} = 300\,000$ nm). (d) Transverse damage zone mechanism ($k = 15$, $p = 13$, $K_I = 209.4$ GPa$\sqrt{\text{nm}}$, $w_{SM} = 28\,000$ nm, $l_{SM} = 300\,000$ nm).
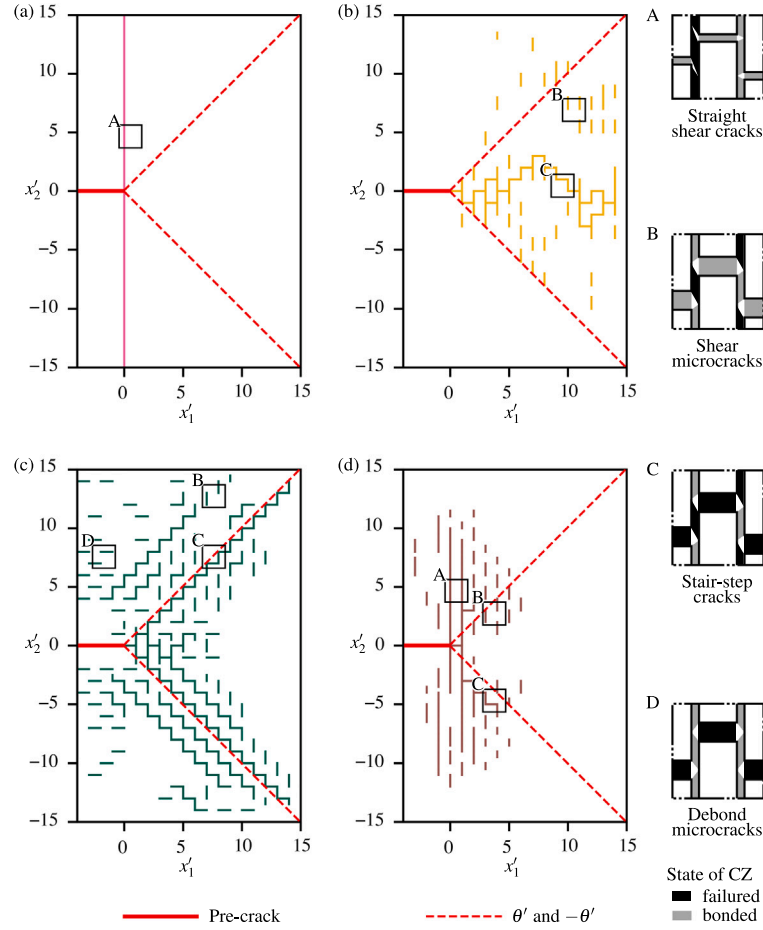
Fig. 9. Four distinct failure mechanisms shown as the normalized crack morphology: (a) Delamination cracking mechanism ($k = 2$, $p = 20$, $K_I = 14.5$ GPa$\sqrt{\text{nm}}$). (b) Longitudinal damage zone mechanism ($k = 2$, $p = 1$, $K_I = 41.7$ GPa$\sqrt{\text{nm}}$). (c) Crack bifurcation mechanism ($k = 15$, $p = 1$, $K_I = 151.6$ GPa$\sqrt{\text{nm}}$). (d) Transverse damage zone mechanism ($k = 15$, $p = 13$, $K_I = 209.4$ GPa$\sqrt{\text{nm}}$). Typical microcracking mechanisms on the cohesive zones within square regions denoted as A, B, C, D are schematically illustrated on the right side of the figure. A: Straight shear cracks, B: Shear microcracks, C: Stair-step cracks, D: Debond microcracks.

3.2. Evaluation of toughness and effects of process zone

The J–integral (Rice, 1968)

$$J = \int_C \left(W \delta_{j1} - \sigma_{ij} \frac{\partial u_i}{\partial x_1} \right) m_j \, ds \tag{13}$$

is used to assess the fracture toughness of the nacre-like materials. The path C represents a contour surrounding the crack tip, W is the strain energy density, and δ_{ij} is the identity tensor and m_j is the outward normal vector of the integration path C. The integration path is set within the homogenized CM to ensure that all the energy dissipation occurs within the contour. Furthermore, the equivalent domain integral (EDI) method facilitates the implementation of J–integral in finite element analysis (Li et al., 1985). Because there is no energy dissipation within the CM, the J–integral is theoretically path-independent in the CM, which is confirmed through computational experiments, as shown in Fig. B.1. Moreover, the computational solutions agree with the theoretical solution of energy release rate for the orthotropic elasticity (Sih et al., 1965)

$$G_I = K_I^2 \sqrt{\frac{b_{11} b_{22}}{2}} \left[\sqrt{\frac{b_{22}}{b_{11}}} + \frac{2b_{12} + b_{66}}{2b_{11}} \right]^{\frac{1}{2}} \tag{14}$$

This validates the use of the remote J–integral for evaluating the toughness of nacre-like materials.

4. Result and discussion

4.1. Fracture mechanism transition attributed by microstructure

In the first part of this section, we describe the impact of microstructure on the fracture mechanisms of nacre-like materials. Tankasala et al. (2017) study the fracture mechanism with competition between crack penetration and crack kinking depends on the orthotropic elasticity even in homogeneous solids. The microstructure of nacre-like materials not only specifies overall anisotropic elasticity but also confines the geometrically admissible paths of microcracks. The influence of the microstructure is examined by controlling the aspect ratio k and the CZ strength ratio p, and we set p in the range from 0 to 30 and k in the range from 2 to 40. The results using finite element analysis show that different microstructures lead to four distinct fracture mechanisms: longitudinal damage zone (LDZ) mechanism, crack bifurcation (CB) mechanism, transverse damage zone (TDZ) mechanism, and delamination cracking (DC) mechanism. These fracture mechanisms are indicated on a failure-mechanism map as shown in Fig. 7. The parameter ranges corresponding to the four fracture mechanisms are illustrated using different color blocks, while the plotted symbols of the corresponding color represent the examined parameters. The characteristics of each fracture mechanism are summarized in schematic diagrams around the map. Furthermore, the actual process zone and crack morphology of the four typical combinations of p and k (red
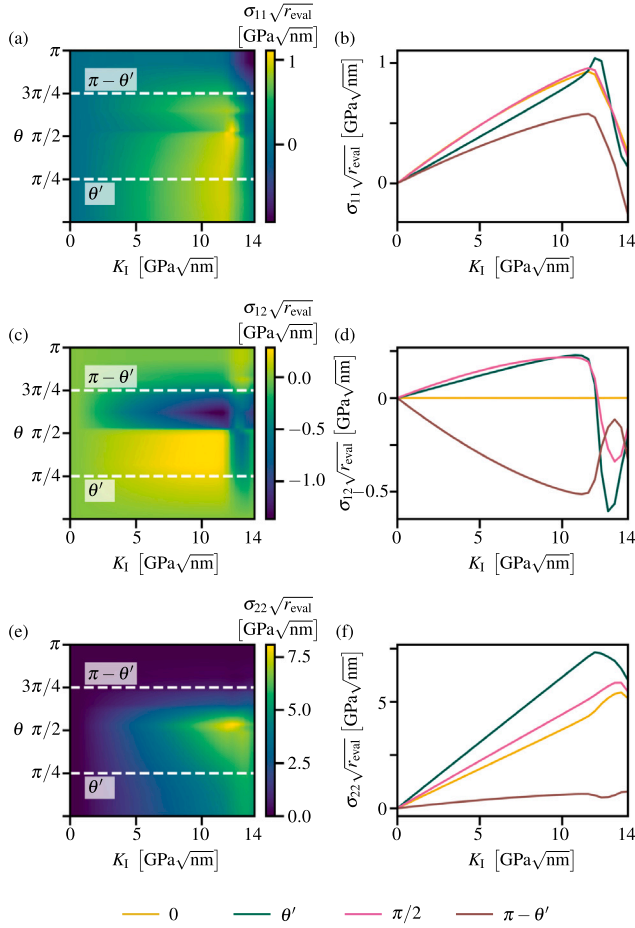
Fig. 10. Variation of the stress field near the crack tip in the DC mechanism with loading $r_{eval} = 2\,000$ nm. (a), (c), (e): Heatmap of stress field. (b), (d), (f): Variation of stress with loading at crucial angles.

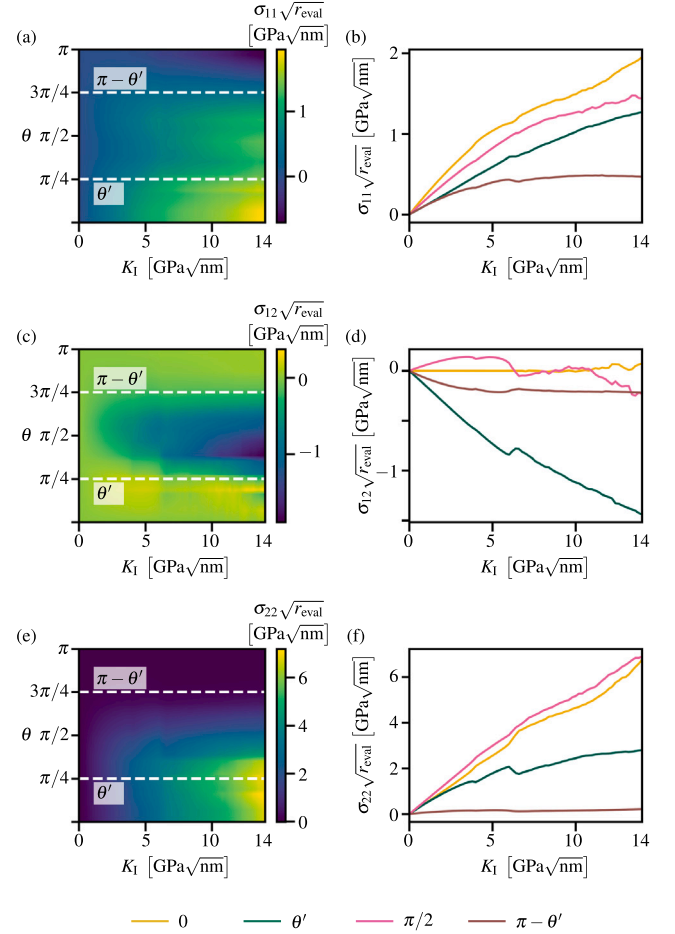**Fig. 11.** Variation of the stress field near the crack tip in the LDZ mechanism with loading $r_{eval} = 2\,000$ nm. (a), (c), (e): Heatmap of stress field. (b), (d), (f): Variation of stress with loading at crucial angles.

circles in Fig. 7) are illustrated in Figs. 8 and 9 to provide more details on the difference between fracture mechanisms. In Fig. 8, the deformation behavior of the process zone is illustrated by the damage factor D. Therefore, the shape, size, and compactness of the process zone can be visually confirmed by referring to Fig. 8. In Fig. 9, we show the crack morphology by drawing damaged CZs with line segments. The dimensions for x_1 and x_2 axes are scaled based on the geometric dimensions of the tablet, $x'_1 = x_1/w$, $x'_2 = 2x_2/l$, to expose the topological characters of the crack morphology unaffected by difference of tablets' aspect ratio. Consequently, any arbitrary staggered structure is mapped onto an ideal isometric grid with the crack tip fixed at $(0,0)$. In addition, typical microcracking mechanisms on the cohesive zones within square regions denoted A, B, C, D are schematically illustrated, in which A, B, C, D correspond to straight shear cracks, shear microcracks, stair-step cracks, debond microcracks, respectively.

The characteristics of all four fracture mechanisms can be summarized as follows, based on Figs. 8 and 9:

- **Longitudinal damage zone (LDZ) mechanism**
  Within the yellow parameter range in the map's bottom left corner in Fig. 7, where both k and p are small, the model shows the LDZ mechanism. This fracture mechanism is the one that occurs the most frequently in natural nacre-like materials. In Fig. 8(b) and Fig. 9(b), the distinctive feature is a fan-shaped sizable process zone before the crack tip. Furthermore, the damage in the region between θ' and $-\theta'$ is significantly higher

compared to other regions. This suggests that the nacre-like materials' staggered microstructure helps prevent stress concentration at the crack tip, delaying crack propagation. This observation aligns with the experimental results reported by Rabiei et al. (2010). At the macroscopic level, the crack propagation direction parallels the pre-crack. However, the crack continues to deflect and develops a zigzag-like crack path. These deflections can significantly increase the material's toughness, as stated by Song et al. (2018) and Abid et al. (2019). Furthermore, many microcracks are observed near the main crack, indicating more energy dissipation (Rabiei et al., 2010; Song et al., 2018).

- **Crack bifurcation (CB) mechanism**
  A sizable process zone is observed surrounding the crack tip in this mechanism, as shown in Fig. 8(c) and Fig. 9(c). However, the region in front of the crack tip is protected, and θ' and $-\theta'$ directions are where the process zone develops. The presence of stair-step cracks that branch along the θ' and $-\theta'$ directions is the main characteristic of this fracture mechanism. This phenomenon of crack bifurcation was similarly observed in the experimental study conducted by Yahyazadehfar and Arola (2015). The existence of sub-cracks parallel to the main crack but unconnected is another distinguishing feature. These sub-cracks significantly increase the material's toughness (Schmahl et al., 2012).

- **Transverse damage zone (TDZ) mechanism**
  The TDZ mechanism appears when the model has a large aspect ratio k and improved strength of the interlayer connections, making crack propagation along the direction perpendicular to the
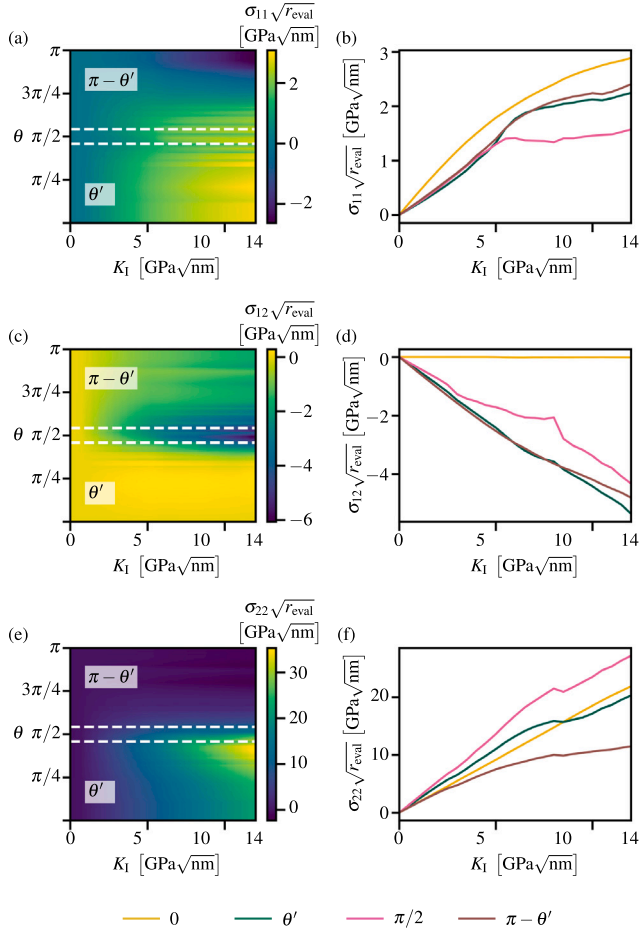
Fig. 12. Variation of the stress field near the crack tip in the CB mechanism with loading $r_{\mathrm{eval}} = 8\,000$ nm. (a), (c), (e): Heatmap of stress field. (b), (d), (f): Variation of stress with loading at crucial angles.
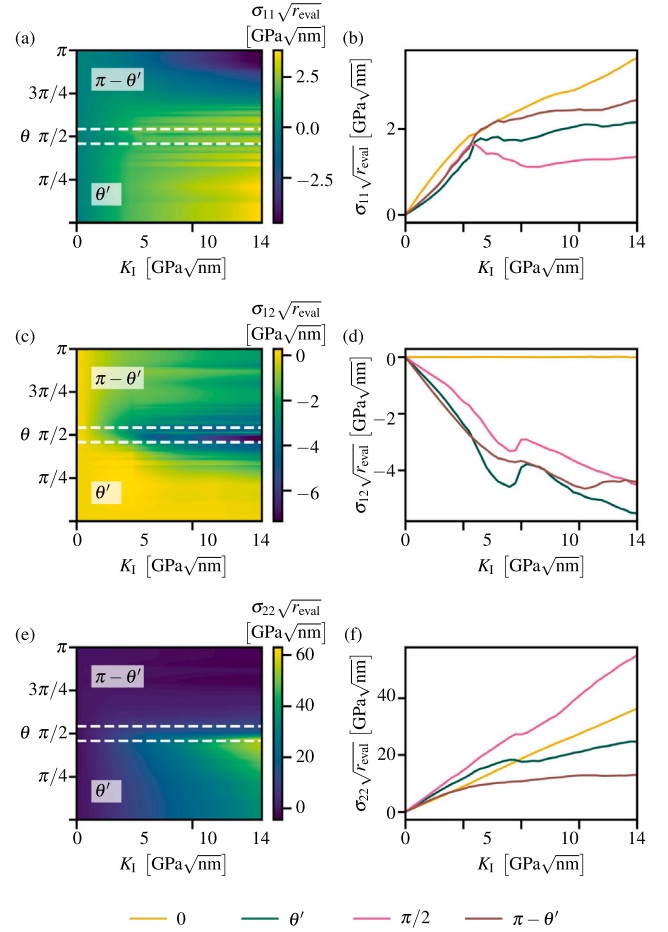
Fig. 13. Variation of the stress field near the crack tip in the TDZ mechanism with loading $r_{\mathrm{eval}} = 8\,000$ nm. (a), (c), (e): Heatmap of stress field. (b), (d), (f): Variation of stress with loading at crucial angles.

tablet extremely difficult. The process zone in the TDZ mechanism is divided into two symmetric parts, just similar to the CB mechanism. However, the process zone in the TDZ mechanism further concentrates between θ' and $\pi - \theta'$, as shown in Fig. 8(d) and Fig. 9(d). The TDZ mechanism's highly complex crack morphology is characterized by transverse cracks connected to the main crack and parallel sub-cracks. Additionally, a significant number of microcracks are also observed.

- **Delamination cracking (DC) mechanism**

  If the influence of parameters k and p on fracture mechanisms observed above can be generalized to the parameter range shown in the top left corner of Fig. 7, then the mechanism within this region should exhibit characteristics between LDZ and TDZ. However, the results obtained from the finite element analysis do not support this conjecture. The crack transversely propagates through the protein matrix, leading to the DC mechanism with a single straight crack parallel to the tablet, as shown in Fig. 8(a) and Fig. 9(a). No spread process zone is observed around the crack tip, compared with the other three fracture mechanisms, indicating that almost all energy dissipation is used to propagate the single straight crack. The commonly observed toughening mechanisms in nacre-like materials, such as microcrack and crack bifurcation, are ineffective within this parameter range. The potential risks caused by this loss of process zone and toughening mechanisms will be illustrated in the following discussion on toughness.

We highlight the transition of fracture mechanisms controlled by the microstructure and confirm that larger aspect ratios and stronger intralayer connections can induce crack deflection away from the pre-crack direction. However, the influence of the microstructure on the fracture behavior extends beyond these observations. When both k and p are small, the model exhibits the LDZ mechanism. The CB mechanism obtained by increasing k and the TDZ mechanism obtained by increasing both k and p exhibit features similar to those of the basic LDZ mechanism. These features include a large process zone, complex crack morphology, and activation of multiple toughening mechanisms, although there are some differences in the details, such as different shapes of the process zone and different activated mechanisms. In contrast, a unique DC mechanism is generated when p is increased, where no toughening mechanisms are activated and no process zone is observed.

4.2. Stress field near the crack tip

Then, the stress field of each fracture mechanism near the crack tip is presented. The stress fields evaluated at a distance r_{eval} from the crack tip in the Cartesian coordinate system for the four fracture mechanisms as they change with loading are shown in Figs. 10–13. We normalize the stress field using $\sqrt{r_{\mathrm{eval}}}$ to eliminate the influence of the radius. However, as shown in Figs. 14–17, the relationship between stress and angle under specific loading is presented to illustrate the transition from an elastic stress field dominated by K_{I} to a stress field
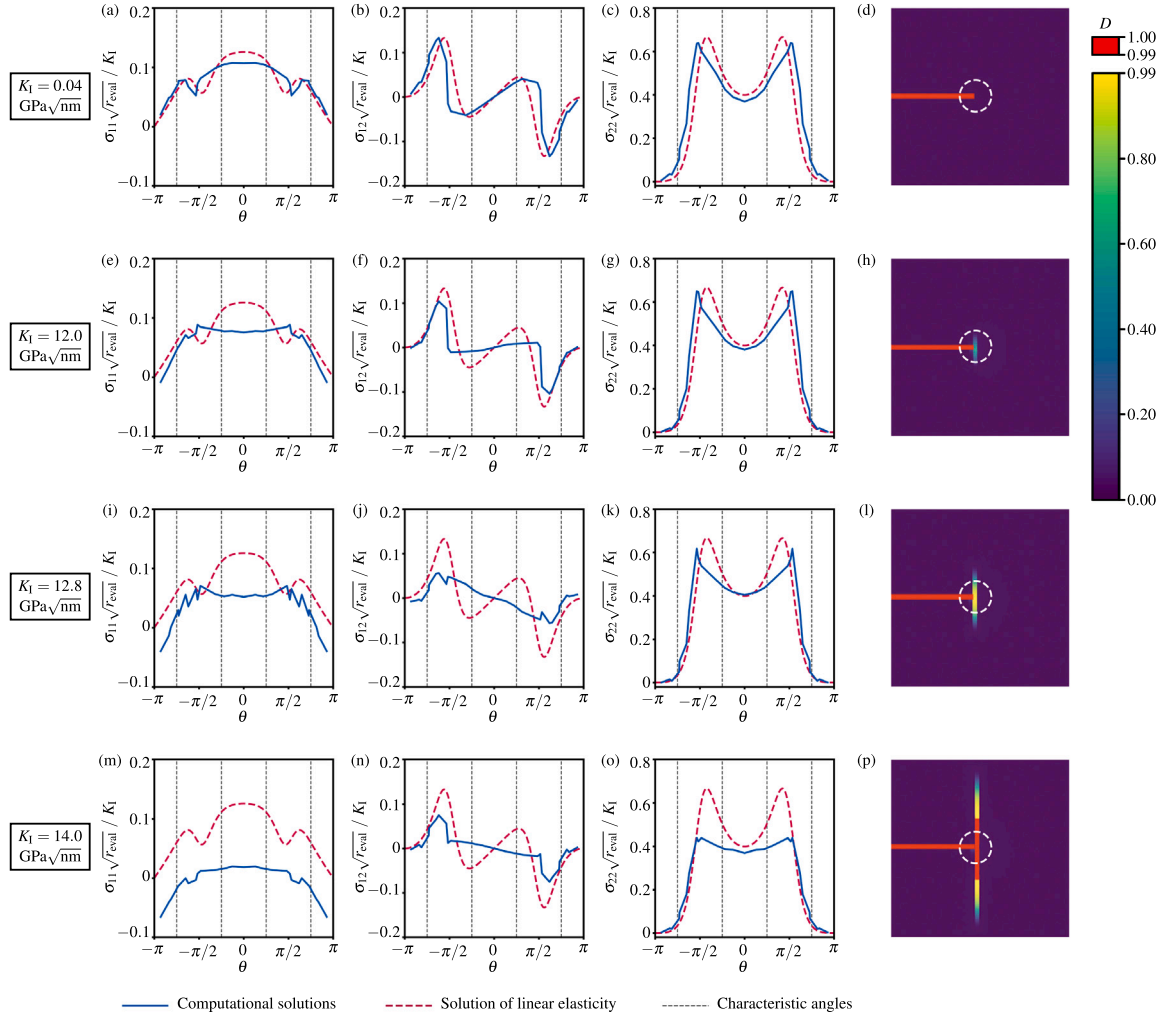
Fig. 14. Stress field near the crack tip and damage distribution in the DC mechanism, under specific loading ($r_{\mathrm{eval}} = 2\,000$ nm).

dominated by nonlinear deformation with more details. Moreover, the state of the process zone is presented. In Figs. 14–17, the stress fields are normalized by $\sqrt{r_{\mathrm{eval}}}/K_{\mathrm{I}}$ and compared with the theoretical crack tip stress field for linear elastic orthotropic materials, as shown in Eq. (11). The stresses are obtained by interpolating the stresses at the integration points of the tablet elements. We set $r_{\mathrm{eval}} = 2\,000$ nm for the models with aspect ratios of 2 (LDZ, DC) and $r_{\mathrm{eval}} = 8\,000$ nm for the models with aspect ratios of 15 (TDZ, CB) to ensure an adequate number of points to describe the near-tip field, owing to the significant influence of the aspect ratio on the size of the tablet. The distribution of the process zone under a specific load is also presented to establish the relationship between nonlinear deformation behavior and the stress field.

As shown in Figs. 10–17, the different microstructures result in distinct linear elastic fracture mechanical stress fields for the four fracture mechanisms. However, they exhibit similar shape character-istics. In the early stages of loading, the computational solutions of the stress fields in all mechanisms closely match the theoretical solu-tions, indicating that the initial stress field is dominated by K_{I}. This consistency demonstrates the validity of simplifying the remote CM as orthotropic material. However, the nonlinear deformation of the inter-faces near the crack tip results in deviations between the computational and theoretical solutions as the loading increases. A nonlinear region gradually replaces the singularity-dominated region described by K_{I}.

Moreover, the different process zone characteristics of different fracture mechanisms result in distinctly different stress fields near the crack tip.

In the DC mechanism, the damage is highly concentrated in the matrix on both sides of the crack tips. Consequently, the stress field, or stress gradient field exhibits discontinuities at $\theta = \pm \pi/2$, as shown in Fig. 14. Furthermore, rapid crack propagation accompanied by rapid stress redistribution is observed when K_{I} exceeds 12 GPa$\sqrt{\mathrm{nm}}$, as shown in Fig. 10. Within the range of $-\pi/2$ to $\pi/2$, both σ_{11} and σ_{12} decrease and approach zero after the crack propagation, with a temporary reversal observed in σ_{12}. In addition, σ_{22} becomes nearly constant within this range.

In the LDZ mechanism, a distinct process zone is formed within a sector at the crack tip with increasing loading. This results in a reduction in the stress concentration near the crack tip, manifested by a significant decrease in σ_{11} and σ_{12} within this range. The tablets within this range experience a similar stress state, as shown in Fig. 15. Despite the generation of the process zone, σ_{22} remains higher than the theoretical elastic solution and significantly higher than the other mechanisms within the range of $-\theta'$ to θ', leading to crack propagation within this range. In addition, a discontinuity in the stress field along $\pm\theta'$ is observed, which is consistent with the findings of Pro et al. (2015a).

In the CB mechanism, the process zone is primarily concentrated near $-\theta'$ and θ', resulting in a significant discontinuity of stress near
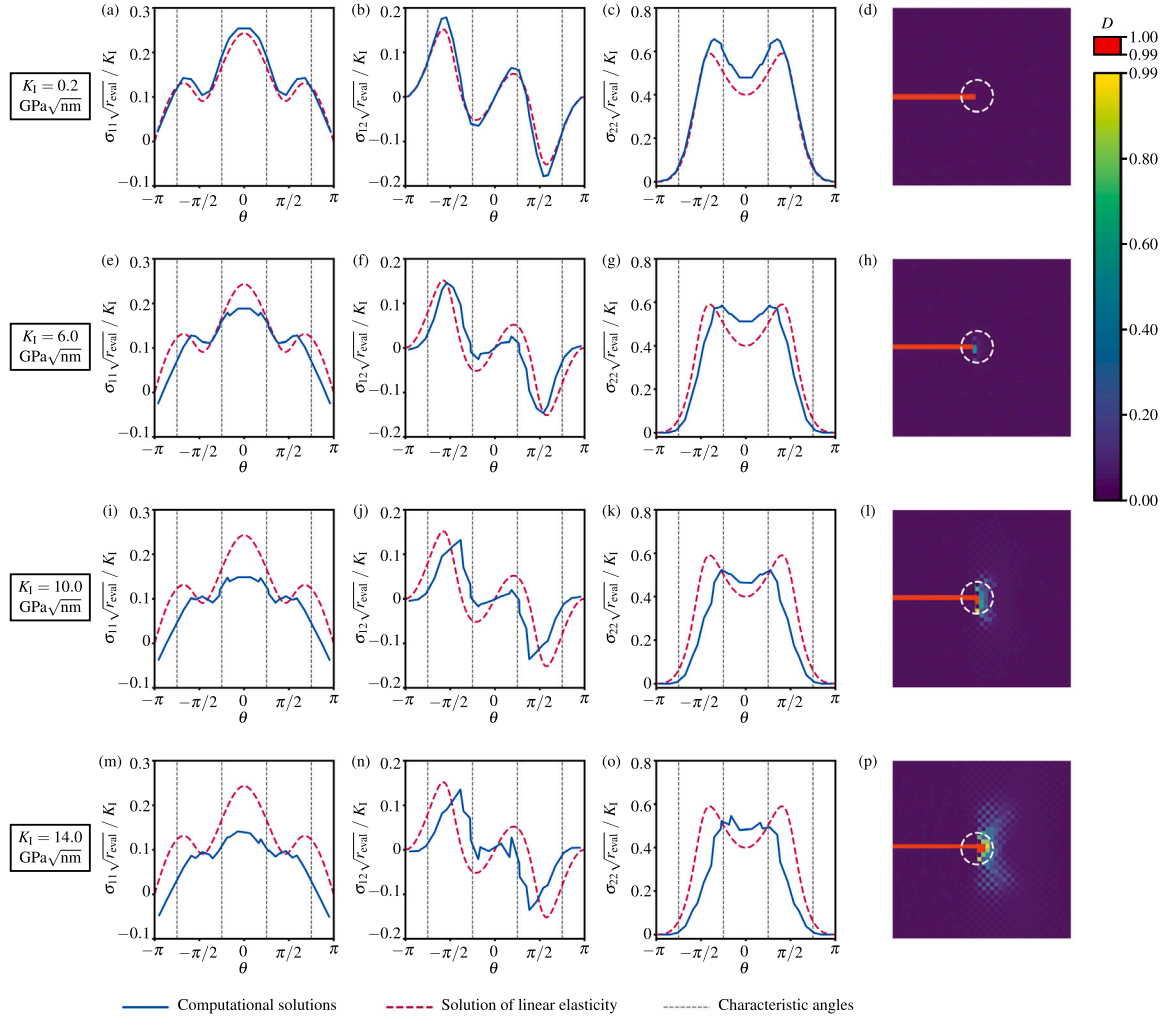
Fig. 15. Stress field near the crack tip and damage distribution in the LDZ mechanism, under specific loading ($r_{\mathrm{eval}} = 2\,000$ nm).

$\pm\theta'$ due to the separation between the tablets. Within the range $-\theta'$ to θ', both σ_{11} and σ_{12} are almost constant and maintain at low levels, whereas σ_{22} still closely matches the elastic solution, as shown in Fig. 16.

In the TDZ mechanism, the process zone is primarily distributed between θ' and $\pi - \theta'$, and a stress discontinuity is observed in this range, as shown in Fig. 17. However, because of the large aspect ratio, θ' approaches $\pi/2$, and the difference in the stress field between TDZ and CB mechanisms is insignificant.

4.3. Toughening attributed by microstructure

The influence of the fracture mechanisms on the toughness is revealed by the fracture resistance (R–curve) of the four typical parameter combinations mentioned above, as shown in Fig. 18. Crack propagation a is commonly chosen as the variable of the horizontal axis in the R–curve plot. In this study, however, we extend the conventional R–curve plot to a 3D plot to clarify the mechanism of toughening due to the staggered structure. Considering that the staggered structure constrains the crack path to the matrix, the crack path can be divided into segments parallel to x_1 or x_2 direction, as shown in Fig. 9. The minimum unit of crack propagation corresponds to the width w of the tablet in the x_1 direction and corresponds to the length of the half-tablet $l/2$ in the x_2 direction. Therefore, we define dimensionless crack

propagation b_1 and b_2, and the crack propagation can be described as the crack propagates through b_1 layers in the x_1 direction and b_2 half-tablets in the x_2 direction. Then we extend the original two-dimensional R–curve to a three-dimensional R–curve, as shown in Fig. 18(a), where the z-axis represents the fracture toughness J, and the x_1-axis and x_2-axis represent dimensionless crack propagation components b_1 and b_2, respectively. This plot demonstrates the variation in fracture toughness associated with crack propagation in a staggered structure. Figs. 18(b) and (c) show the projections of Fig. 18(a) onto the J–b_2 and J–b_1 planes, respectively, and indicate the crack resistance in the x_2 and x_1 directions. Considering the application scenarios of nacre-like materials, preventing crack propagation perpendicular to the tablets is necessary. Thus, we consider the resistance of cracks propagating along the x_1-direction, as shown in Fig. 18(c), as the fracture toughness of nacre-like materials. Fig. 18(d) shows the projection of Fig. 18(a) onto the b_1–b_2 plane, illustrating the crack propagation process as the trajectory of moving point (b_1, b_2).

Fig. 18 demonstrates that the LDZ, CB, and TDZ mechanisms all exhibit excellent fracture toughness, with rising R–curve as the crack propagates. This rising resistance can prevent unstable crack propagation and catastrophic failures. The highest fracture toughness is observed for the TDZ mechanism. Distinct large stairs can be observed in the crack resistance curve, as shown in Fig. 18(c). For instance, the value of J must increase from 38.0 J/m^2 to 566.2 J/m^2, implying
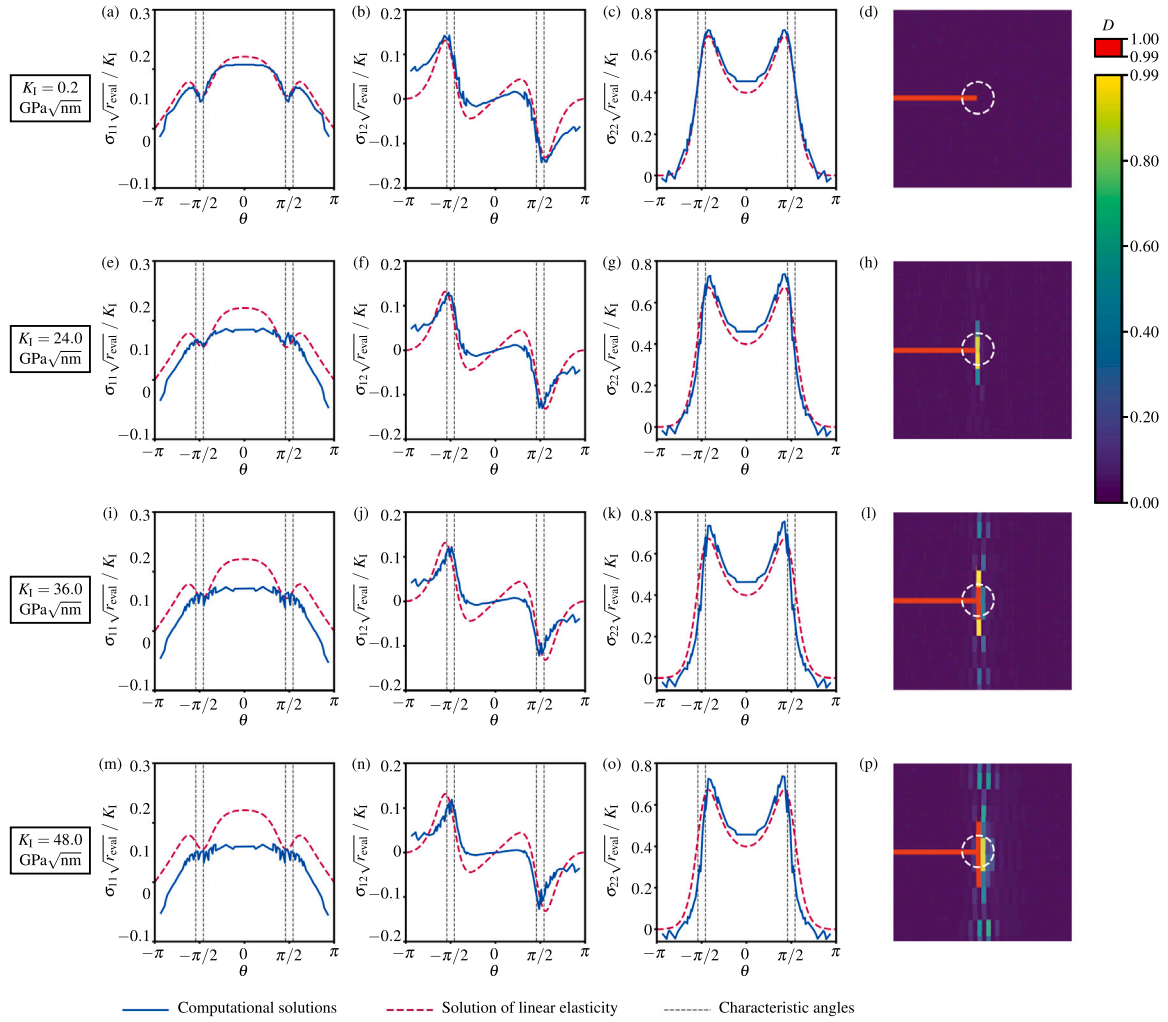
Fig. 16. Stress field near the crack tip and damage distribution in the CB mechanism, under specific loading ($r_{\text{eval}} = 8\,000$ nm).

that crack propagation along the x_1 direction encounters significant resistance, to increase b_1 from 1 to 2. These large stairs can be deduced from Figs. 18(b) and (d), which are the result of the crack's transverse propagation. The energy input is dissipated during the generation of the surface of the transverse cracks, significantly delaying the propagation in the x_1 direction and improving the toughness. Furthermore, the CB mechanism produces a higher fracture toughness than the LDZ mechanism because of the increased crack surface area caused by the larger aspect ratio and complex crack morphology, such as bifurcation and sub-cracks. Notably, even the LDZ mechanism, which had the lowest toughness among the three, still exhibits a notable overall toughness compared to both interfaces.

Fig. 18 shows a significant decrease in fracture toughness in the DC mechanism. The DC mechanism exhibits zero x_1-direction crack propagation, indicating infinite crack resistance in this direction. However, this is meaningless because extremely poor toughness immediately results in a catastrophic failure in the x_2 direction, as shown in Fig. 18(b). This low toughness can be attributed to several factors, as shown in Figs. 8 and 9, including the absence of a process zone, evident stress concentration, straight crack path, and deactivated toughening mechanisms. Therefore, in the design of artificial nacre-like materials, increasing the strength of intralayer connections should be avoided because this may lead to the occurrence of the DC mechanism and extremely poor toughness.

In conclusion, our research highlights the fracture mechanisms of nacre-like materials and their pronounced sensitivity to microstructural variations, particularly with respect to levels of anisotropy and the mechanical properties of interfaces. These findings demonstrate that transition of fracture mechanisms significantly influences the macroscopic toughness of the materials.

5. Conclusions

This study investigated the small-scale failure process of nacre-like materials, and established a connection between microstructures and macroscopic mechanical properties. We demonstrated that alterations in the microstructure of nacre-like materials significantly affected the fracture mechanisms and stress fields near the crack tips, resulting in a significant impact on the overall toughness. The near-tip field behavior of nacre-like materials is investigated using finite element analysis. The key conclusions are summarized as follows.

In this study, we employed a homogenized model to achieve simulations at the scale of millions of tablets while balancing accuracy and computational cost. This method can easily be applied to other soft and hard materials.

Furthermore, under small-scale failure assumption, the nacre-like materials exhibited four distinct fracture mechanisms as the microstructure changed. These fracture mechanisms exhibit different process zone
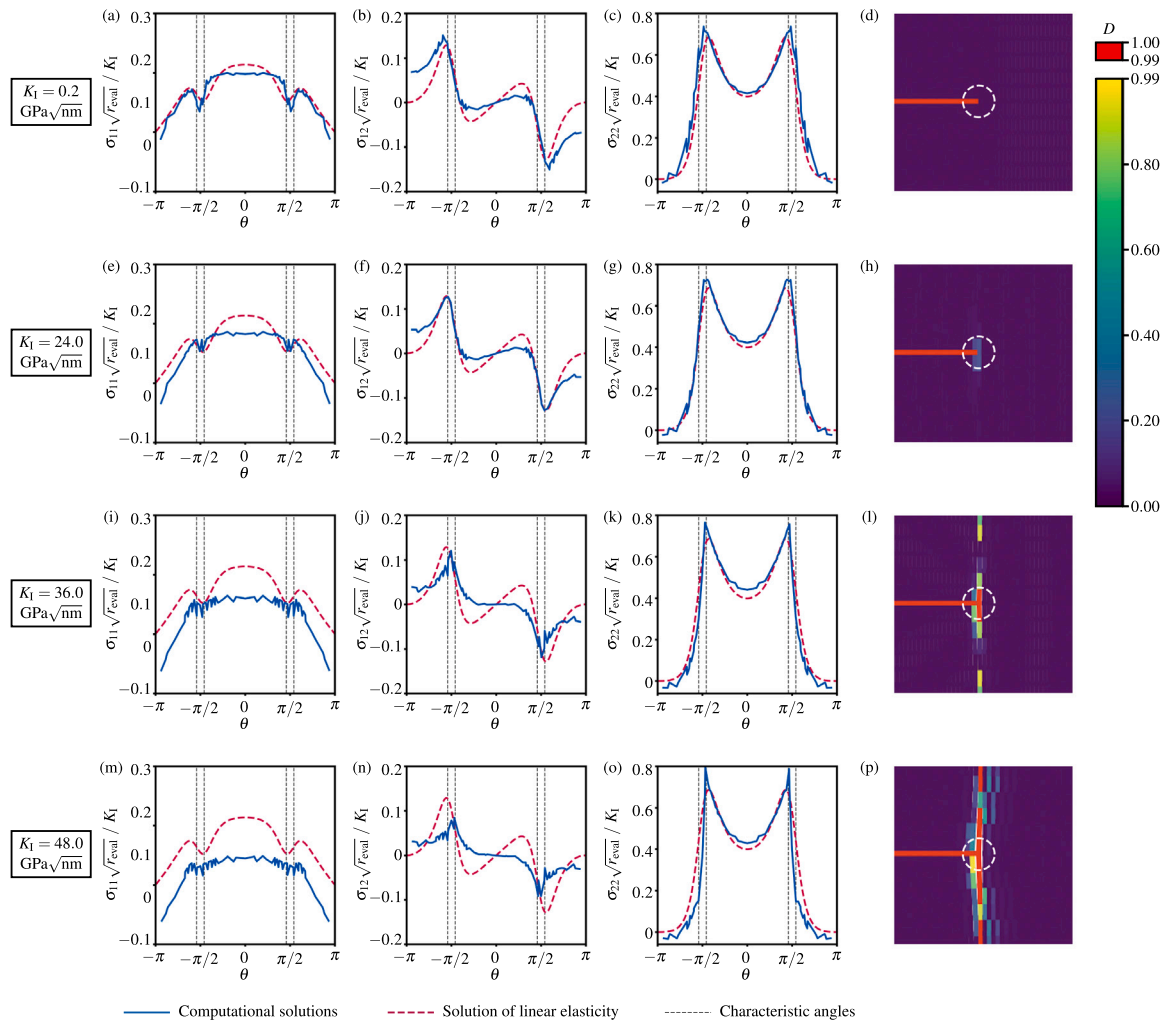
Fig. 17. Stress field near the crack tip and damage distribution in the TDZ mechanism, under specific loading ($r_{\text{eval}} = 8\,000$ nm).

characteristics, crack morphologies, and near-tip fields, resulting in significantly different levels of toughness that differed by hundreds of times in magnitude. A failure-mechanism map that would be a chart for material design is proposed to indicate the fracture mechanisms.

This study deepens the understanding of how the microstructure of nacre-like materials influences their overall mechanical properties. A new design strategy for artificial nacre-like materials is presented, involving the design of the microstructure to induce specific fracture mechanisms and activate specific toughening mechanisms to achieve optimal toughness.

It is noteworthy that, for simplicity, in this study, several assumptions regarding the interface were adopted. While these assumptions facilitated the research process, they may have also overlooked certain factors critical to understanding the nacre-like materials' fracture mechanisms. Further investigation in this area remains valuable and necessary.

CRediT authorship contribution statement

Xiaoyan Ye: Writing – review & editing, Writing – original draft, Software, Methodology, Investigation, Data curation, Conceptualization. **Akihiro Nakatani:** Writing – review & editing, Writing – original draft, Supervision, Software, Resources, Project administration, Methodology, Funding acquisition, Conceptualization.

Declaration of competing interest

The authors declare that they have no known competing financial interests or personal relationships that could have appeared to influence the work reported in this paper.

Data availability

Data will be made available on request.

Declaration of generative AI and AI-assisted technologies in the writing process

During the preparation of this study, the authors used ChatGPT to enhance the language quality and readability of the manuscript. After using this tool, the authors reviewed and edited the content as needed and took full responsibility for the publication.
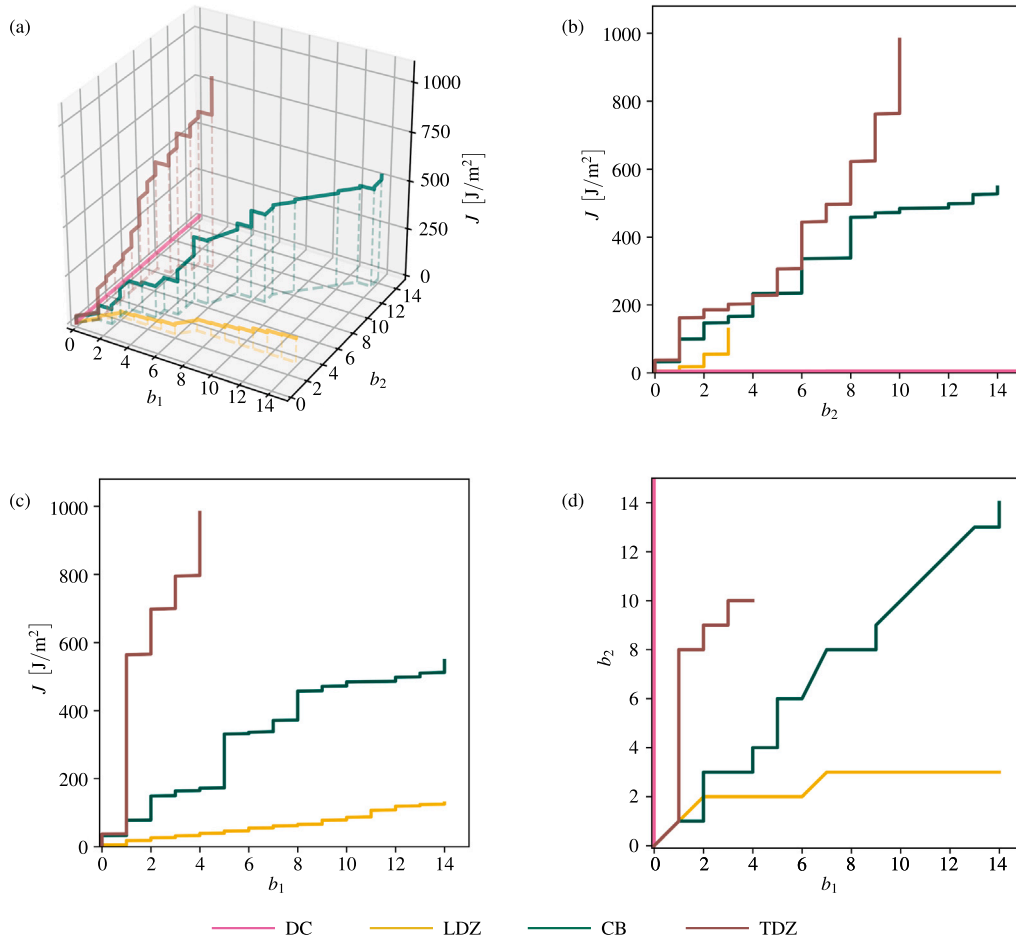
Acknowledgments

Fig. 18. Crack resistance curve for different fracture mechanisms: (a) 3D plot of R–curve. (b) The variation of J with respect to b_2. (c) The variation of J with respect to b_1, which is considered as fracture toughness of nacre-like material. (d) Crack propagation process illustrated by the movement of points (b_1, b_2).

Professor Yusuke Doi (Osaka University) for the fruitful discussions. The authors would like to thank Editage (www.editage.com) for editing and reviewing this manuscript for English language.

Appendix A. Evaluation of homogenized elasticity property

In the planar problem of orthotropic materials, the relationship between strain ε_{11}, ε_{22}, $\gamma_{12} = 2\varepsilon_{12}$ and stress σ_{11}, σ_{22}, σ_{12} can be expressed as

$$\begin{bmatrix} \varepsilon_{11} \\ \varepsilon_{22} \\ \gamma_{12} \end{bmatrix} = \begin{bmatrix} b_{11} & b_{12} & 0 \\ b_{21} & b_{22} & 0 \\ 0 & 0 & b_{66} \end{bmatrix} \begin{bmatrix} \sigma_{11} \\ \sigma_{22} \\ \sigma_{12} \end{bmatrix} \tag{A.1}$$

In this study, the compliance matrix b_{IJ} of orthotropic materials under plane strain conditions is obtained by subjecting a model with a staggered structure to three independent deformation components, as shown in Fig. A.1. The subscripts IJ of the matrix denote Voigt notation, and the matrix components b_{11}, b_{12}, b_{21}, b_{22}, b_{66} in Eq. (A.1) correspond to the tensor components b_{1111}, b_{1122}, b_{2211}, b_{2222}, $b_{1212}(= b_{1221} = b_{2112} = b_{2121})$, respectively. The strains are specified within a small range, allowing CZ to be approximated as linear elastic response.
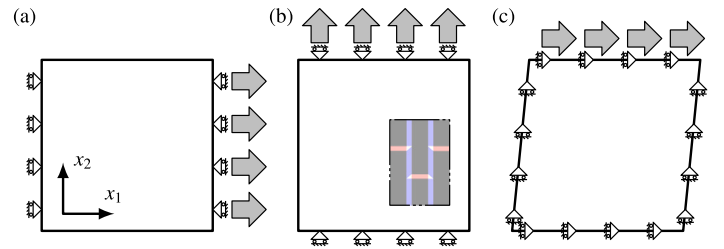

Fig. A.1. Three deformation modes of the trial experiment used to determine the elastic constants: (a) Uniaxial stretching loading along the x_1-direction, $\sigma_{22} = \sigma_{12} = 0$; (b) Uniaxial stretching loading along the x_2-direction, $\sigma_{11} = \sigma_{12} = 0$; (c) Pure shear loading, $\sigma_{11} = \sigma_{22} = 0$.

Upon uniaxial stretching along the x_1-direction, as shown in Fig. A.1(a), $\sigma_{22} = \sigma_{12} = 0$, we obtain the value of b_{11}, b_{12} by

$$b_{11} = \frac{\varepsilon_{11}}{\sigma_{11}}, \quad b_{12} = \frac{\varepsilon_{22}}{\sigma_{11}} \tag{A.2}$$

Similarly, the values of b_{21}, b_{22}, b_{66} are evaluated.

Appendix B. Validation of small-scale yielding model

The path independence of the J–integral in CM is shown in Fig. B.1, and the computational solutions agree with the theoretical solutions, demonstrating that using the remote J–integral to assess material
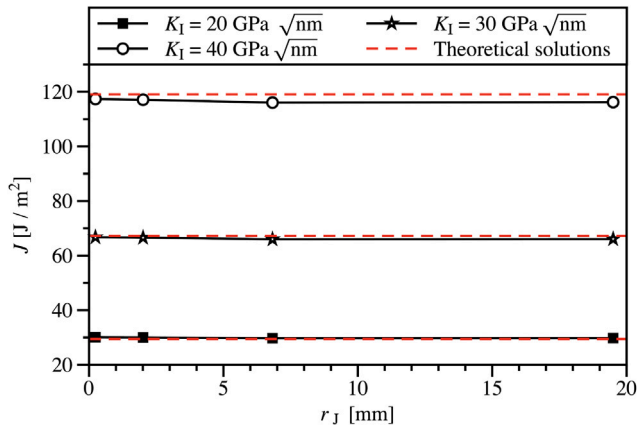
Fig. B.1. The J–integral remains path independent within the CM throughout the entire loading process ($k = 2$, $p = 1$). r_J denotes the radius of the circular J–integral path.
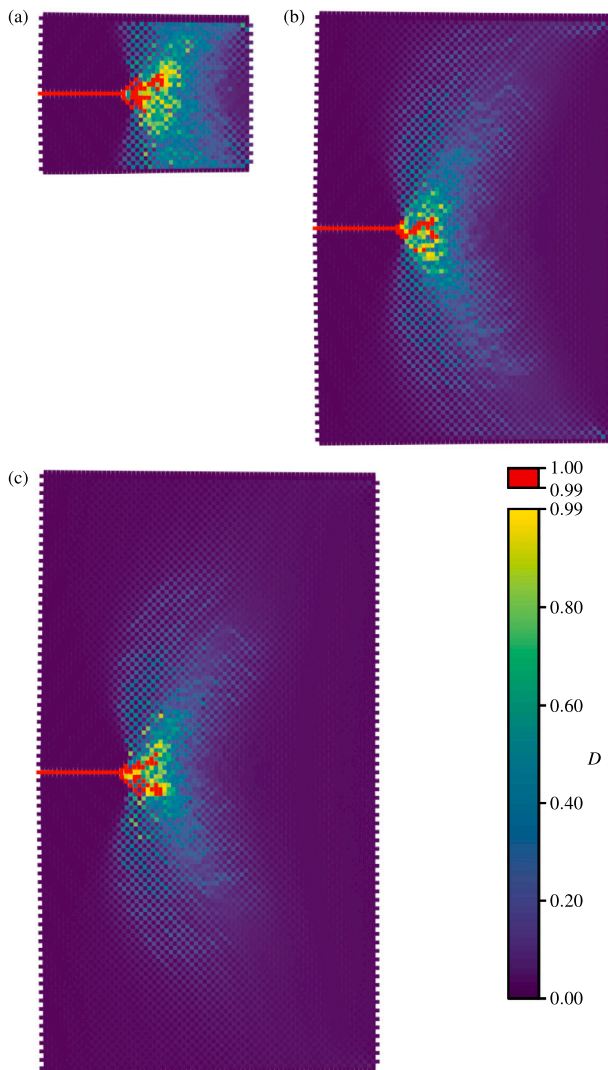

Fig. B.3. Models with different SM sizes exhibiting similar rising resistance curves.

Fig. B.2. Fracture mechanism and process zone showing the independence of the SM size ($K = 40$ GPa$\sqrt{\text{nm}}$): (a) 18×50 ($w_{SM} = 20\,000$ nm, $l_{SM} = 14\,400$ nm). (b) 50×70 ($w_{SM} = 28\,000$ nm, $l_{SM} = 40\,000$ nm). (c) 70×80 ($w_{SM} = 32\,000$ nm, $l_{SM} = 56\,000$ nm).

toughness is appropriate in the SSY model. r_j represents the distance from the integrated path to the pre-crack tip.

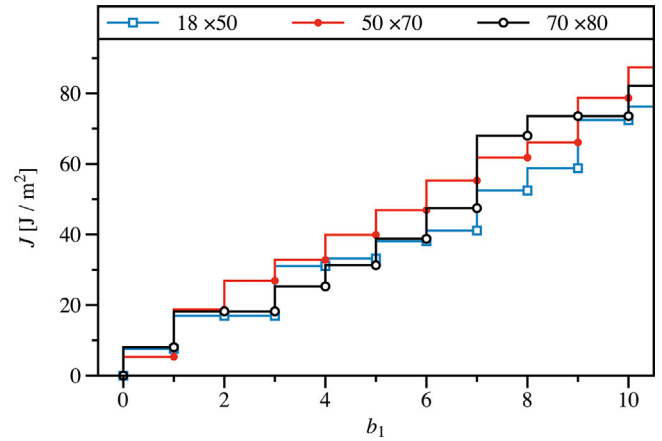Additionally, we assume that all nonlinear deformations occurred within the SM while simplifying the elastic region far from the crack tip as a homogeneous orthotropic material to reduce computational costs. However, this approximation introduces errors. To ensure the validity of the SSY model, we confirm that the fracture mechanisms and toughness are independent of the SM size, as shown in Figs. B.2 and B.3. We select three model sizes: 18×50, 50×70, and 70×80. The first number represents the number of tablets in each layer and the second number represents the number of layers within the SM. The parameters $k = 2$ and $p = 1$ are kept constant in all the models, whereas the other parameters are listed in Table 1. According to Figs. B.2 and B.3, we can observe that the three models with different sizes of SM all exhibit the same LDZ fracture mechanism and display similar toughness and rising resistance curves. Notably, in the 18×50 model, the development of the process zone is noticeably influenced by the homogenized boundaries, indicating that the influence of the homogenized boundary is limited to the vicinity of the boundaries and did not have a significant impact on the fracture behavior at the crack tip. Furthermore, from Fig. B.2(b) and (c), we can observe that the damage of the CZs near the homogenized boundary can be neglected, confirming the validity of the results for these SM sizes. In conclusion, the validity of the results obtained for the SM with size 50×70 used in this study is demonstrated.

References

Abid, N., Mirkhalaf, M., Barthelat, F., 2018. Discrete-element modeling of nacre-like materials: Effects of random microstructures on strain localization and mechanical performance. J. Mech. Phys. Solids 112, 385–402. http://dx.doi.org/10.1016/j.jmps.2017.11.003.

Abid, N., Pro, J.W., Barthelat, F., 2019. Fracture mechanics of nacre-like materials using discrete-element models: Effects of microstructure, interfaces and randomness. J. Mech. Phys. Solids 124, 350–365. http://dx.doi.org/10.1016/j.jmps.2018.10.012.

Barthelat, F., 2010. Nacre from mollusk shells: A model for high-performance structural materials. Bioinspir. Biomimet. 5, 035001. http://dx.doi.org/10.1088/1748-3182/5/3/035001.

Barthelat, F., Espinosa, H., 2007. An experimental investigation of deformation and fracture of nacre–mother of pearl. Exp. Mech. 47 (3), 311–324. http://dx.doi.org/10.1007/s11340-007-9040-1.

Barthelat, F., Li, C.-M., Comi, C., Espinosa, H.D., 2006. Mechanical properties of nacre constituents and their impact on mechanical performance. J. Mater. Res. 21 (8), 1977–1986. http://dx.doi.org/10.1557/jmr.2006.0239.

Barthelat, F., Rabiei, R., 2011. Toughness amplification in natural composites. J. Mech. Phys. Solids 59 (4), 829–840. http://dx.doi.org/10.1016/j.jmps.2011.01.001.

Barthelat, F., Tang, H., Zavattieri, P., Li, C.-M., Espinosa, H., 2007. On the mechanics of mother-of-pearl: A key feature in the material hierarchical structure. J. Mech. Phys. Solids 55 (2), 306–337. http://dx.doi.org/10.1016/j.jmps.2006.07.007.

Begley, M.R., Philips, N.R., Compton, B.G., Wilbrink, D.V., Ritchie, R.O., Utz, M., 2012. Micromechanical models to guide the development of synthetic 'brick and mortar' composites. J. Mech. Phys. Solids 60 (8), 1545–1560. http://dx.doi.org/10.1016/j.jmps.2012.03.002.

Bertoldi, K., Bigoni, D., Drugan, W., 2008. Nacre: An orthotropic and bimodular elastic material. Compos. Sci. Technol. 68 (6), 1363–1375. http://dx.doi.org/10.1016/j.compscitech.2007.11.016.

Cleveringa, H., Van der Giessen, E., Needleman, A., 2000. A discrete dislocation analysis of mode I crack growth. J. Mech. Phys. Solids 48 (6–7), 1133–1157. http://dx.doi.org/10.1016/S0022-5096(99)00076-9.

Gao, H., Ji, B., Jäger, I.L., Arzt, E., Fratzl, P., 2003. Materials become insensitive to flaws at nanoscale: Lessons from nature. Proc. Natl. Acad. Sci. 100 (10), 5597–5600. http://dx.doi.org/10.1073/pnas.0631609100.

Ji, B., Gao, H., 2004. Mechanical properties of nanostructure of biological materials. J. Mech. Phys. Solids 52 (9), 1963–1990. http://dx.doi.org/10.1016/j.jmps.2004.03.006.

Kruzic, J.J., Nalla, R.K., Kinney, J.H., Ritchie, R., 2003. Crack blunting, crack bridging and resistance-curve fracture mechanics in dentin: Effect of hydration. Biomaterials 24 (28), 5209–5221. http://dx.doi.org/10.1016/s0142-9612(03)00458-7.

Li, X., Chang, W.-C., Chao, Y.J., Wang, R., Chang, M., 2004. Nanoscale structural and mechanical characterization of a natural nanocomposite material: The shell of red abalone. Nano Lett. 4 (4), 613–617. http://dx.doi.org/10.1021/nl049962k.

Li, F.Z., Shih, C.F., Needleman, A., 1985. A comparison of methods for calculating energy release rates. Eng. Fract. Mech. 21 (2), 405–421. http://dx.doi.org/10.1016/0013-7944(85)90029-3.

Lin, A.Y.-M., Meyers, M.A., 2009. Interfacial shear strength in abalone nacre. J. Mech. Behav. Biomed. Mater. 2 (6), 607–612. http://dx.doi.org/10.1016/j.jmbbm.2009.04.003.

Maghsoudi-Ganjeh, M., Lin, L., Yang, X., Zeng, X., 2021. Computational modeling and simulation of bioinspired nacre-like composites. J. Mater. Res. 36, 2651–2661. http://dx.doi.org/10.1557/s43578-021-00124-6.

Mayer, G., 2006. New classes of tough composite materials—Lessons from natural rigid biological systems. Mater. Sci. Eng.: C 26 (8), 1261–1268. http://dx.doi.org/10.1016/j.msec.2005.08.031.

Menig, R., Meyers, M., Meyers, M., Vecchio, K., 2000. Quasi-static and dynamic mechanical response of haliotis rufescens (abalone) shells. Acta Mater. 48 (9), 2383–2398. http://dx.doi.org/10.1016/S1359-6454(99)00443-7.

Meyers, M.A., Lin, A.Y.-M., Chen, P.-Y., Muyco, J., 2008. Mechanical strength of abalone nacre: Role of the soft organic layer. J. Mech. Behav. Biomed. Mater. 1 (1), 76–85. http://dx.doi.org/10.1016/j.jmbbm.2007.03.001.

Nakatani, A., Drugan, W., Van der Giessen, E., Needleman, A., 2003. Crack tip fields at a ductile single crystal-rigid material interface. Int. J. Fract. 122, 131–159. http://dx.doi.org/10.1023/B:FRAC.0000005775.10890.43.

Nejati, M., Ghouli, S., Ayatollahi, M.R., 2021. Crack tip asymptotic fields in anisotropic planes: Importance of higher order terms. Appl. Math. Model. 91, 837–862. http://dx.doi.org/10.1016/j.apm.2020.09.025.

Pro, J.W., Lim, R.K., Petzold, L.R., Utz, M., Begley, M.R., 2015a. GPU-based simulations of fracture in idealized brick and mortar composites. J. Mech. Phys. Solids 80, 68–85. http://dx.doi.org/10.1016/j.jmps.2015.03.011.

Pro, J.W., Lim, R.K., Petzold, L.R., Utz, M., Begley, M.R., 2015b. The impact of stochastic microstructures on the macroscopic fracture properties of brick and mortar composites. Extreme Mech. Lett. 5, 1–9. http://dx.doi.org/10.1016/j.eml.2015.09.001.

Rabiei, R., Bekah, S., Barthelat, F., 2010. Failure mode transition in nacre and bone-like materials. Acta Biomater. 6 (10), 4081–4089. http://dx.doi.org/10.1016/j.actbio.2010.04.008.

Rice, J.R., 1968. A path independent integral and the approximate analysis of strain concentration by notches and cracks. J. Appl. Mech. 35 (2), 379–386. http://dx.doi.org/10.1115/1.3601206.

Roychowdhury, S., Dodds, R.H., 2003. A numerical investigation of 3-D small-scale yielding fatigue crack growth. Eng. Fract. Mech. 70 (17), 2363–2383. http://dx.doi.org/10.1016/S0013-7944(03)00003-1.

Sarikaya, M., Gunnison, K., Yasrebi, M., Aksay, I., 1989. Mechanical property-microstructural relationships in abalone shell. MRS Online Proc. Libr. 174, 109–116. http://dx.doi.org/10.1557/PROC-174-109.

Schmahl, W.W., Griesshaber, E., Kelm, K., Goetz, A., Jordan, G., Ball, A., Xu, D., Merkel, C., Brand, U., 2012. Hierarchical structure of marine shell biomaterials: Biomechanical functionalization of calcite by brachiopods. Z. Kristallogr.-Cryst. Mater. 227 (11), 793–804. http://dx.doi.org/10.1524/zkri.2012.1542.

Shao, Y., Zhao, H.-P., Feng, X.-Q., 2014. On flaw tolerance of nacre: A theoretical study. J. R. Soc. Interface 11 (92), 20131016. http://dx.doi.org/10.1098/rsif.2013.1016.

Sih, G.C., Paris, P., Irwin, G., 1965. On cracks in rectilinearly anisotropic bodies. Int. J. Fract. Mech. 1 (3), 189–203. http://dx.doi.org/10.1007/BF00186854.

Song, J., Fan, C., Ma, H., Liang, L., Wei, Y., 2018. Crack deflection occurs by constrained microcracking in nacre. Acta Mech. Sin. 34, 143–150. http://dx.doi.org/10.1007/s10409-017-0724-1.

Sun, J., Bhushan, B., 2012. Hierarchical structure and mechanical properties of nacre: A review. RSC Adv. 2, 7617–7632. http://dx.doi.org/10.1039/c2ra20218b.

Tankasala, H.C., Deshpande, V.S., Fleck, N.A., 2017. Crack kinking at the tip of a mode I crack in an orthotropic solid. Int. J. Fract. 207 (2), 181–191. http://dx.doi.org/10.1007/s10704-017-0227-x.

Tsai, H.-C., Chen, C.-H., Shu, Y.-C., 2021. Crack behavior in nacre-like composites: A phase-field method. In: Bioinspiration, Biomimetics, and Bioreplication XI, vol. 11586, SPIE, 1158608. http://dx.doi.org/10.1117/12.2582658.

Vashishth, D., 2004. Rising crack-growth-resistance behavior in cortical bone: Implications for toughness measurements. J. Biomech. 37 (6), 943–946. http://dx.doi.org/10.1016/j.jbiomech.2003.11.003.

Wang, R., Gupta, H.S., 2011. Deformation and fracture mechanisms of bone and nacre. Annu. Rev. Mater. Res. 41, 41–73. http://dx.doi.org/10.1146/annurev-matsci-062910-095806.

Wang, R.Z., Suo, Z., Evans, A.G., Yao, N., Aksay, I.A., 2001. Deformation mechanisms in nacre. J. Mater. Res. 16, 2485–2493. http://dx.doi.org/10.1557/jmr.2001.0340.

Wang, R., Wen, H., Cui, F., Zhang, H., Li, H., 1995. Observations of damage morphologies in nacre during deformation and fracture. J. Mater. Sci. 30, 2299–2304. http://dx.doi.org/10.1007/BF01184577.

Xie, Z., Yao, H., 2014. Crack deflection and flaw tolerance in "brick-and-mortar" structured composites. Int. J. Appl. Mech. 6 (02), 1450017. http://dx.doi.org/10.1142/S1758825114500173.

Xu, X.-P., Needleman, A., 1994. Numerical simulations of fast crack growth in brittle solids. J. Mech. Phys. Solids 42 (9), 1397–1434. http://dx.doi.org/10.1016/0022-5096(94)90003-5.

Yahyazadehfar, M., Arola, D., 2015. The role of organic proteins on the crack growth resistance of human enamel. Acta Biomater. 19, 33–45. http://dx.doi.org/10.1016/j.actbio.2015.03.011.

Yan, Y., Nakatani, A., 2019a. Stability controlled crack initiation in nacre-like composite materials. J. Mech. Phys. Solids 125, 591–612. http://dx.doi.org/10.1016/j.jmps.2019.01.003.

Yan, Y., Nakatani, A., 2019b. Unlocalized crack initiation and propagation in staggered biomaterials. J. Biomech. 86, 183–192. http://dx.doi.org/10.1016/j.jbiomech.2019.02.003.

Yan, Y., Nakatani, A., 2020. Crack sensitivity of nacre-like laminate composite materials: Monte Carlo simulation based on stability theory. Int. J. Solids Struct. 202, 646–659. http://dx.doi.org/10.1016/j.ijsolstr.2020.06.043.

Yan, Y., Zhao, Z.-L., Feng, X.-Q., Gao, H., 2022. Nacre's brick–mortar structure suppresses the adverse effect of microstructural randomness. J. Mech. Phys. Solids 159, 104769. http://dx.doi.org/10.1016/j.jmps.2021.104769.

Zavattieri, P.D., Hector, L.G., Bower, A.F., 2008. Cohesive zone simulations of crack growth along a rough interface between two elastic–plastic solids. Eng. Fract. Mech. 75 (15), 4309–4332. http://dx.doi.org/10.1016/j.engfracmech.2007.11.007.